Dependencies of high-latitude plasma convection: Consideration of interplanetary magnetic field, seasonal, and universal time factors in statistical patterns

J. M. Ruohoniemi and R. A. Greenwald
Johns Hopkins University Applied Physics Laboratory, Laurel, Maryland, USA

Received 28 September 2004; revised 28 February 2005; accepted 8 April 2005; published 1 September 2005.

[1] The database of the nine radars of the Super Dual Auroral Radar Network (SuperDARN) in the northern hemisphere has been analyzed for information on factors that influence the convection of plasma in the high-latitude ionosphere. The velocity measurements were collected over the period 1998–2002. The data were first used to derive a new statistical model of convection that improves upon the earlier one-radar model of Ruohoniemi and Greenwald (1996) in its specification of the dependence of the convection pattern on the magnitude and direction of the IMF in the GSM Y-Z plane. We then derived average patterns for secondary sortings by season, year, and radar. Such dependencies as emerged were most clearly seen by contrasting the results for B_y+ and B_y-. The seasonal effect in the convection pattern is found to have similarities to that of the sign of B_y. In particular, the combination of B_y+/summer (B_y-/winter) reinforces the tendency of the B_y sign factor to sculpt the dusk and dawn cells into more round/crescent (crescent/round) shapes and to shift the crescent cell across the midnight MLT meridian. However, these combinations are associated with lower estimates of the total cross polar cap potential drop, Φ_{PC}, while the nonreinforcing combinations produce elevated Φ_{PC}, especially B_y-/summer. There is an overall tendency for Φ_{PC} to increase from winter to summer, although the pure seasonal effect on the potential drop is weaker than that of the B_y-sign/season factor. We did not find pronounced differences among the patterns derived for the 5 individual years, which spanned the most recent interval of solar cycle maximum. Sorting by radar, we found few differences among the patterns for B_y+, but for B_y-, variations emerged that are consistent with a possible dependence on universal time (UT). The impacts of season and UT on convection in the high-latitude ionosphere thus depends on the IMF, especially the sign of B_y. We speculate that variability in the ionospheric conductivity has a greater effect on magnetosphere-ionosphere coupling under B_y- conditions.

Citation: Ruohoniemi, J. M., and R. A. Greenwald (2005), Dependencies of high-latitude plasma convection: Consideration of interplanetary magnetic field, seasonal, and universal time factors in statistical patterns, *J. Geophys. Res.*, *110*, A09204, doi:10.1029/2004JA010815.

1. Introduction

[2] The plasma of the high-latitude ionosphere is kept in motion by processes that couple energy and momentum from the solar wind into Earth's magnetosphere. The large-scale pattern of plasma circulation most often conforms to a two-cell configuration with antisunward flow across the pole returning to the dayside via the dawn and dusk flanks. The size and configuration of the pattern and the intensity of the plasma flows are strongly linked to the interplanetary magnetic field (IMF) carried by the solar wind plasma. The reconnection hypothesis of *Dungey* [1961], subsequently developed by workers such as *Crooker* [1979] and *Reiff and Burch* [1985], accounts for the IMF factor by shifting the location of energized plasma flows across the magnetopause according to the requirement that coupling occur where the magnetic fields of the magnetosheath and magnetosphere are antiparallel. For the case of a southward orientation of the interplanetary magnetic field (IMF), or B_z-, reconnection is favored on the subsolar magnetopause near the noon MLT meridian. For azimuthal IMF, i.e., B_y+ or B_y-, the site of reconnection in the northern hemisphere shifts duskward or dawnward, respectively, and ionospheric convection at auroral latitudes in the favored sector acquires a zonal component directed toward noon. In the case of strongly northward IMF, the site of reconnection shifts to higher latitudes and the usual sense of two-cell circulation reverses within small dayside convection cells [*Greenwald et al.*, 1995a]. Even in the absence of IMF, some amount of momentum is transferred across the

0148-0227/05/2004JA010815$09.00

Table 1. SuperDARN Radars–Northern Hemisphere

Radar	Location	Inception	PI	Host Institution
King Salmon	Alaska	2001	T. Kikuchi	Communication Research Laboratory, Japan
Kodiak	Alaska	2000	W. Bristow	University of Alaska Fairbanks, USA
Prince George	British Columbia	2000	G. Sofko	University of Saskatchewan, Canada
Saskatoon	Saskatchewan	1993	G. Sokfo	University of Saskatchewan, Canada
Kapuskasing	Ontario	1993	R. Greenwald	The Johns Hopkins University Applied Physics Laboratory, USA
Goose Bay	Labrador	1983	R. Greenwald	The Johns Hopkins University Applied Physics Laboratory, USA
Stokkseyri	Iceland	1994	J.-P. Villain	Centre National de la Recherche Scientifique, France
Pykkvibaer	Iceland	1995	M. Lester	University of Leicester, UK
Hankasalmi	Finland	1995	M. Lester	University of Leicester, UK

magnetopause by viscous processes and an appreciable zero-level background pattern is maintained [*Papitashvili et al.*, 2002]. The convection is also affected episodically by auroral substorms [*Weimer*, 1999].

[3] There is a lengthy history of efforts to utilize ionospheric measurements to portray the large-scale convection as a function of IMF that goes back at least as far as *Heppner* [1977]. A level of definitiveness was reached with the study of *Heppner and Maynard* [1987]. In the last decade, statistical models were developed by *Rich and Hairston* [1994] using DMSP satellite data, *Weimer* [1995] using DE satellite data, and *Ruohoniemi and Greenwald* [1996] using ground-based HF radar data. Despite the differences in their approaches, these models largely agree in their depiction of the basic IMF dependencies of the global convection. Less direct measurements with ground-based magnetometers have also been applied [*Friis-Christensen et al.*, 1985; *Papitashvili et al.*, 1994; *Ridley et al.*, 2000]. The recent study by *Papitashvili and Rich* [2002] generated a fully parameterized model based on DMSP data and compared the current models in their characterization of the total cross polar cap potential variation, Φ_{PC}, as a function of IMF and season. The models show some seasonal effect but no consensus has emerged that matches the agreement regarding IMF factors.

[4] In this study we apply the data set of measurements collected with the northern radars of the Super Dual Auroral Radar Network (SuperDARN) to derive an improved model to replace the one-radar model of *Ruohoniemi and Greenwald* [1996] and to characterize secondary dependencies of the convection. The statistics are vastly improved over those of the earlier study (RG96) because of the increase in radars from one to nine and the general availability of upstream IMF data from the ACE satellite. After presenting the new model (RG05), we proceed to sort the database by season, year, and radar. We focus on the connection between the IMF factor and the secondary dependencies, especially that of the sign of B_y. The sorting by year relates to the possible impact of solar cycle factors. The sorting by radar relates to the possibility of a dependence on UT. In the course of a day the offset of the geomagnetic pole from the rotational axis causes the solar illumination across the polar cap and auroral zone to vary and this might perturb the convection.

[5] We emphasize that this study focuses on the properties of the convection in its representation as a statistical mean of a large set of measurements. Another body of work addresses the behavior of the instantaneous convection, e.g., *Greenwald et al.* [1999], *Ruohoniemi et al.* [2002]. The convection on timescales of minutes is known to be quite variable, even for relatively stable IMF conditions [*Bristow et al.*, 2004]. This variability must adversely affect the ability of the models to predict the instantaneous convection. Nonetheless, the general consistency of the recent models in terms of their depictions of IMF dependencies shows that mean, or background, convection patterns can be sensibly determined. An understanding of this reproducible aspect of the convection is necessary as a basis for understanding convection dynamics generally. The statistical approach also gives us a practical means to identify the influence of secondary factors that would not be apparent in instantaneous observations.

2. SuperDARN HF Radars

[6] SuperDARN is an international collaboration involving scientists and funding agencies of over a dozen countries that operates chains of HF radars in both the northern and southern hemispheres. *Greenwald et al.* [1995b] has described the concept of the collaboration and its utility for making large-scale, continuous observations in the high-latitude ionosphere. Software developed mainly by the Johns Hopkins University Applied Physics Laboratory (JHUAPL) is used to operate the radars and to generate data in common formats. Table 1 identifies the northern radars, their institutional affiliations, and dates of inception. The data considered in this study were collected exclusively in the northern hemisphere through the years 1998–2002. This interval encompasses about half the period of the current solar cycle, which reached its peak in 2000–2001.

[7] Figure 1 shows a map of the fields of view of the SuperDARN radars in the north. Usually the radars sweep through scans in azimuth every 1 or 2 min. Except for outages due to equipment malfunction or repair work, the radars operate continuously under computer control. They detect backscatter from ionization irregularities in the ionosphere that have been amplified far above thermal fluctuation levels by plasma instability processes. At *F* region altitudes the predominant motion of these irregularities is due to the $\mathbf{E} \times \mathbf{B}$ drift of the ambient plasma [*Villain et al.*, 1985; *Ruohoniemi et al.*, 1987]. Among other measurements, the Doppler velocity imparted to backscattered HF signal is recorded as a function of time, direction, and range. The SuperDARN radar thus provides snapshots of the line-of-sight component of the plasma convection velocity. Further discussion of the factors that affect the measurement of ionospheric plasma convection with HF radars can be

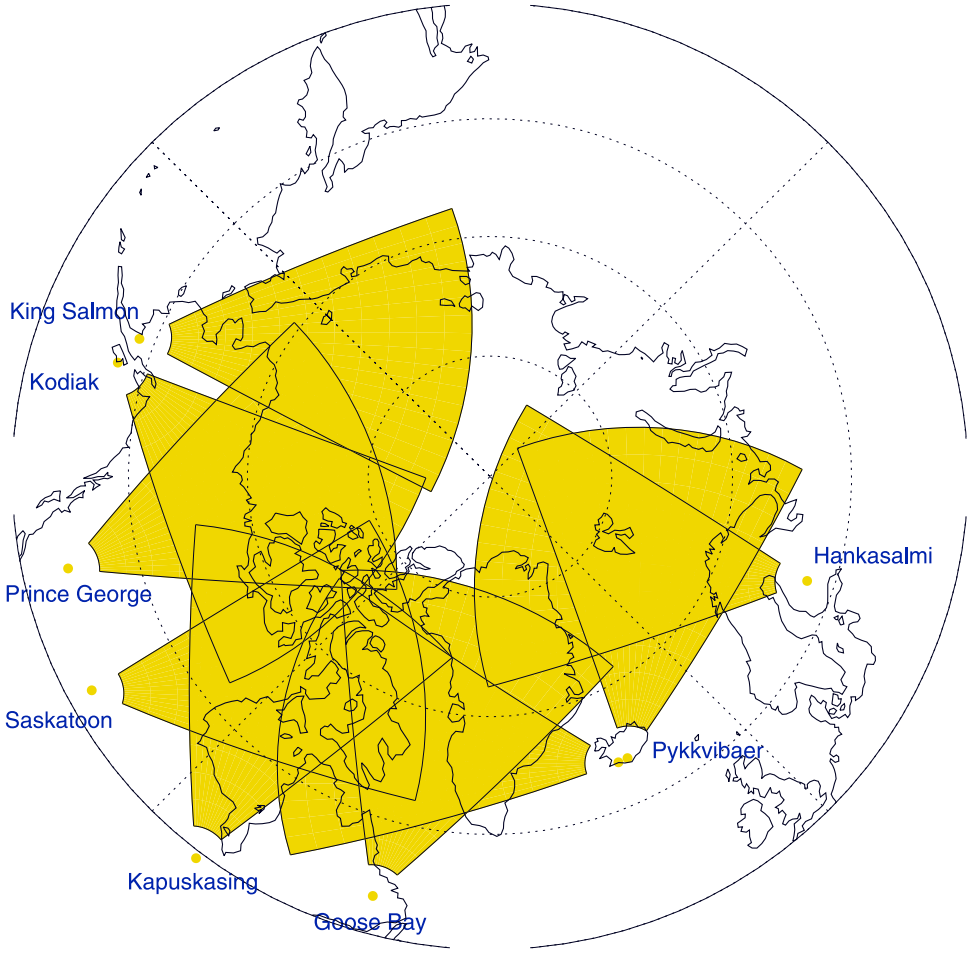

Figure 1. Fields of view of the radars of the SuperDARN collaboration in the northern hemisphere.

found in the work of *Villain et al.* [1984] and *Ruohoniemi and Greenwald* [1997].

3. Data Processing

[8] An assimilative mapping technique has been developed to combine the velocity data from all the radars into a map of the global convection pattern [*Ruohoniemi and Baker*, 1998]. Analysis of time series of convection maps has demonstrated the sensitivity of the instantaneous convection to variations in the IMF [*Greenwald et al.*, 1999; *Ruohoniemi et al.*, 2002]. The technique is also the basis for deriving a nowcast of the convection pattern using data downloaded in near real-time from the northern radars [*Ruohoniemi et al.*, 2001] (available at http://superdarn.jhuapl.edu/). For the work described here it provides a means of reducing global sets of line-of-sight velocity data obtained for selected conditions to estimates of the global distribution of electrostatic potential, Φ, where $\mathbf{E} = -\text{grad}\Phi$.

[9] Our source of information on the IMF is the Advanced Composition Explorer (ACE) MAG instrument. The spacecraft varies its position but is most often situated near the L1 Lagrangian point, which is nearly 200 R_E sunward of the Earth. For this study we are interested in the quasi-static condition of the convection velocity when an IMF condition is known to prevail at the magnetopause. Toward this end, we have performed a rudimentary analysis of the propagation of features in the solar wind from the position of the ACE satellite using the radial component of the solar wind velocity measured by the ACE SWEPAM instrument. When velocity data are selected for an IMF sorting, the conditions must have prevailed at the magnetopause for a period of at least 36 min. We have not specifically included a delay for the pattern to reconfigure following the arrival of an IMF change at the magnetopause; however, our requirement of IMF constancy at the magnetopause easily accommodates the 10–20 min delay that is expected [*Ridley et al.*, 1998]. Owing to the rather longer timescales that are typical of variation in the IMF, the results of the data selection turn out to be insensitive to the details of the propagation/persistence analysis.

[10] In its usual operating mode a SuperDARN radar obtains velocity measurements over the fan-shaped area that is defined by steering the radar beam through 16 successive azimuths with a step of 3.3 deg. Backscattered signal is collected within 75 independent range gates that begin at 180 km and have a separation of 45 km. As shown in Figure 1, the radar fields of view are mainly oriented toward the geomagnetic pole, with the exceptions of the Iceland radars which are directed more zonally. A scan is repeated every 1 or 2 min. Since the resolution available in these measurements exceeds the needs of this statistical study, it is convenient to reduce the data to a coarser format that reduces the data handling requirement and aids in data

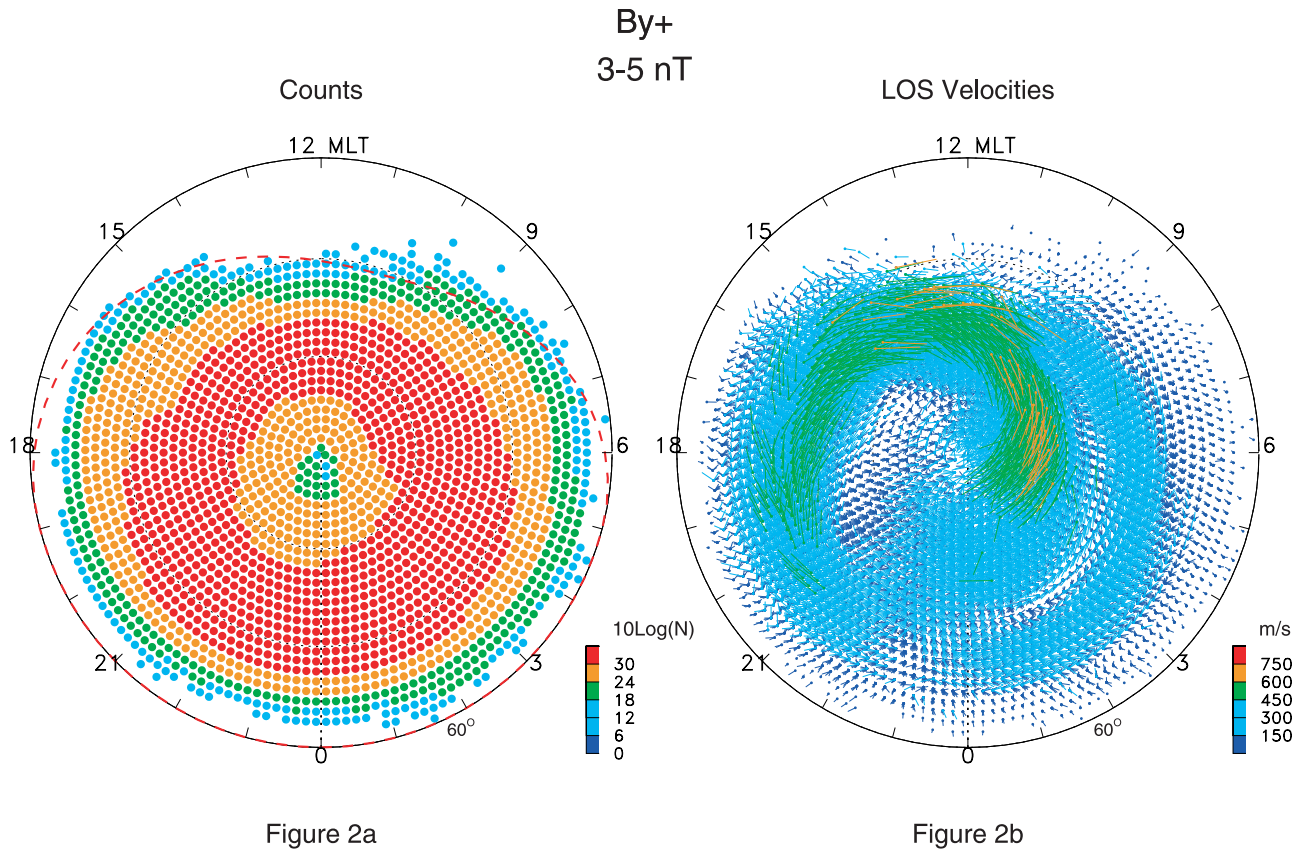

Figure 2. (a) Map of the number of velocity measurements made by the SuperDARN radars for conditions of predominantly IMF B_y+ and magnitude in the 3–5 nT range over the interval 1998–2002. The dashed red line indicates the solution for the equatorward boundary of the convection zone as described in the text. (b) Map of the corresponding binned and averaged line-of-sight velocities.

visualization. First, the velocity data from the individual radars are mapped into a global grid of equal-area cells that is similar to the grid defined by *Ruohoniemi and Baker* [1998] except that the coordinate system is MLT/latitude rather than latitude/longitude. Each cell measures 1 deg in latitude. Within each cell, the velocities are averaged within 10-deg sectors of magnetic azimuth that are centered on azimuths of 0 deg, ±10 deg, ±20 deg, etc. Finally, the data are averaged within 12-min UT intervals. The result is a series of monthly files that summarize the velocity information that is available for reduction to statistical convection maps. These files can be filtered in chronological order for that subset of the records that were collected under specific conditions. As an example, we select those intervals when the IMF magnitude in the GSM *Y-Z* plane was in the 3–5 nT range and the IMF clock angle corresponded to predominantly B_y+ conditions. Figure 2a shows the number of velocity measurements that were obtained within the cells of the mapping grid. The counts reach into the thousands and extend to the pole. Among other features, it is possible to make out some ordering of the distribution by the dayside cusp/cleft geometry [*Ruohoniemi and Greenwald*, 1997]. The aggregate velocity information can be presented in a single plot, as shown in Figure 2b. Each cell within the MLT-latitude grid is populated by a set of velocities at 10-deg step that spans the range of azimuths sampled by the radars. Each velocity represents the statistical mean of the line-of-sight velocity measurement within the given cell in the given direction for the stated IMF conditions.

[11] The derivation of mean line-of-sight velocities generates information on the variability of the velocity measurements. For each setting of position and direction, the root-mean-square scatter of the individual velocity measurements about the mean can be determined. Figure 3a shows a map of variability associated with the velocities of Figure 2b. The variability, depicted here as a scalar function of position, has been obtained by averaging over the magnetic azimuths within each cell. The magnitude of the variability is substantial compared with the mean velocity and its distribution reflects in part the structure of the convection pattern. In future studies we will analyze the behavior of the variability and consider its geophysical significance. Here, we make use of the variability by assigning it as the uncertainty in the associated mean line-of-sight velocity. A fitting analysis can be expected to reproduce the velocities only to within these uncertainties.

[12] Ultimately, we will reduce the set of velocity data to a map of the distribution of the electrostatic potential, Φ. As discussed by *Ruohoniemi and Greenwald* [1998], the result will represent a solution for the data that is optimal in a global sense, that is, the average offset of input and fitted velocities will have been minimized. Alternatively, one can derive a map of the convection that is optimal in a local sense. We briefly consider this option

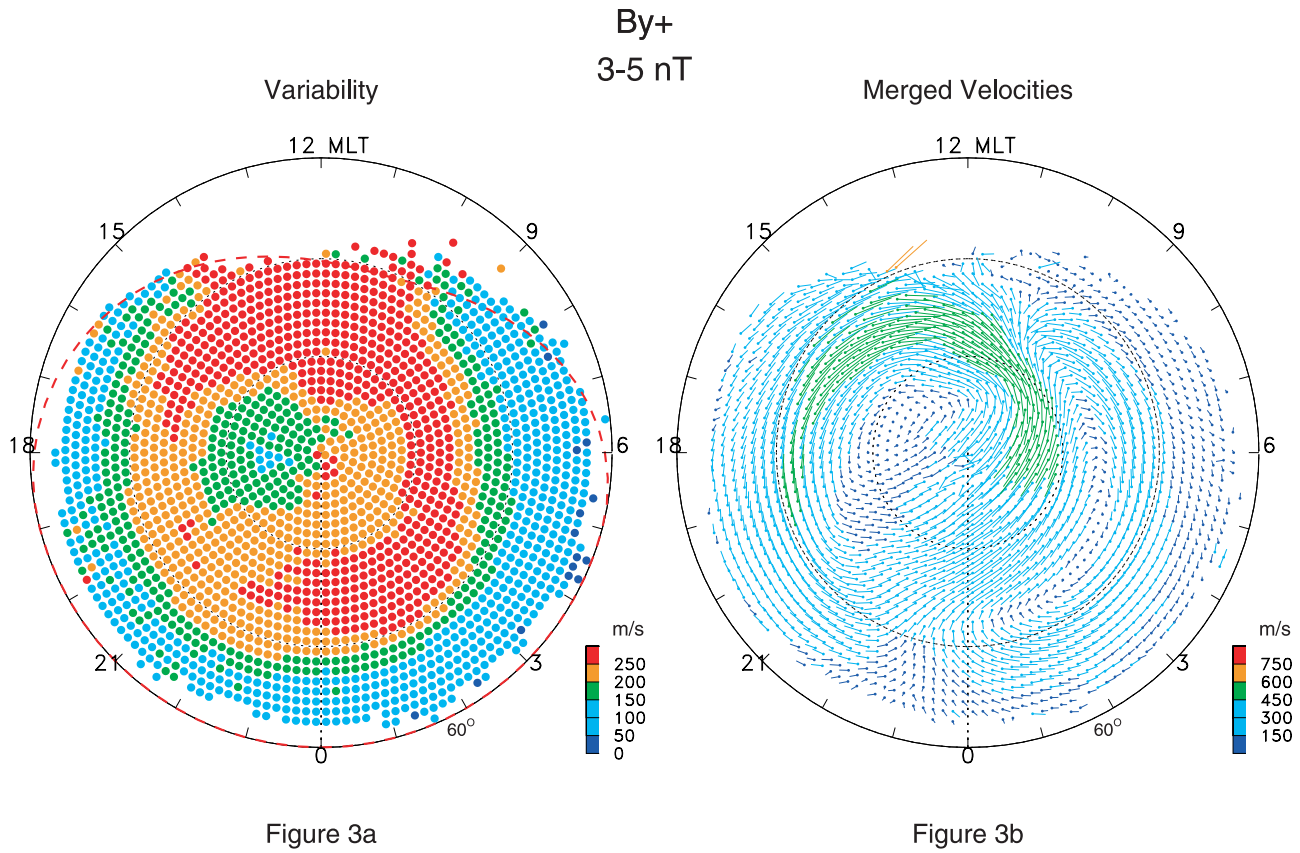

Figure 3. (a) Map of the variability associated with the velocity data presented in Figure 2. (b) Convection velocity vectors obtained by locally solving the variation of the line-of-sight velocity with azimuth.

for the data of Figure 2b. As discussed above, within each grid cell the average value of the line-of-sight component of the convection velocity is expressed as a function of azimuth at 10-deg step. The local velocity vector can be estimated by fitting the velocity variation to a cosine dependence on the azimuth. The result is the map of two dimensional convection velocities shown in Figure 3b. The local solution is of course insensitive to any larger constraints on the convection pattern, such as a condition of zero divergence imposed by the incompressibility of ionospheric plasma. The map shows a two-cell convection pattern with flows circulating within a larger, rounder dusk cell and a distinctively crescent-shaped dawn cell. (Some vectors near the pole are poorly determined owing to the coarseness of the sampling in azimuth there.) The flow magnitude peaks near 600 m/s within the throat-like channel on the dayside. Large-scale features such as the convection reversal boundary (CRB) in the dawn sector can be discerned, indicating a high degree of global coherence across the local velocity determinations.

[13] The most useful representation of the global convection is obtained by solving for the distribution of Φ. The result for this data set is shown in Figure 4a. As described by *Ruohoniemi and Greenwald* [1998], the line-of-sight velocities are fitted to an expansion of Φ in terms of spherical harmonic functions. The spatial resolution is set by the order and degree of the expansion, $L = 8$ and $M = 8$, respectively. For reference, we note that these L and M values are sufficient to exactly reproduce an arbitrary set of velocity measurements distributed along a line (as might be generated by cross-track measurement from a low-altitude satellite) at a spatial step equivalent to the resolution ($\sim$100 km) of the SuperDARN mapping grid. As described above, the uncertainties used in the fitting were taken from the variabilities in the mean line-of-sight velocities. The value of the chi-squared parameter obtained in the fitting was $\chi^2 = 0.2$, indicating that the velocities were, on average, reproduced to well within these uncertainties. Locally, the fitted velocities might be more inconsistent with the measured velocities. To examine this, we have plotted in Figure 4b the convection velocities implied by the solution for the global pattern. This can be compared with the locally optimized velocities shown in Figure 3b. As expected, the local velocities are not exactly reproduced but the overall structure of the convection pattern and the average condition of the flows are quite similar. The global solution renders an estimate for the total cross polar cap potential variation, Φ_{PC}, of 36 kV.

[14] The fitting procedure requires a specification of the equatorward edge of the convection zone, i.e., the position of the zero potential boundary. For mathematical simplicity this boundary is taken to be circular in shape and centered on the geomagnetic pole. Variation in the size of the convection zone is accommodated by adjusting the latitude of the boundary. As discussed by *Shepherd and Ruohoniemi* [2000], the fitting results can be improved by taking into

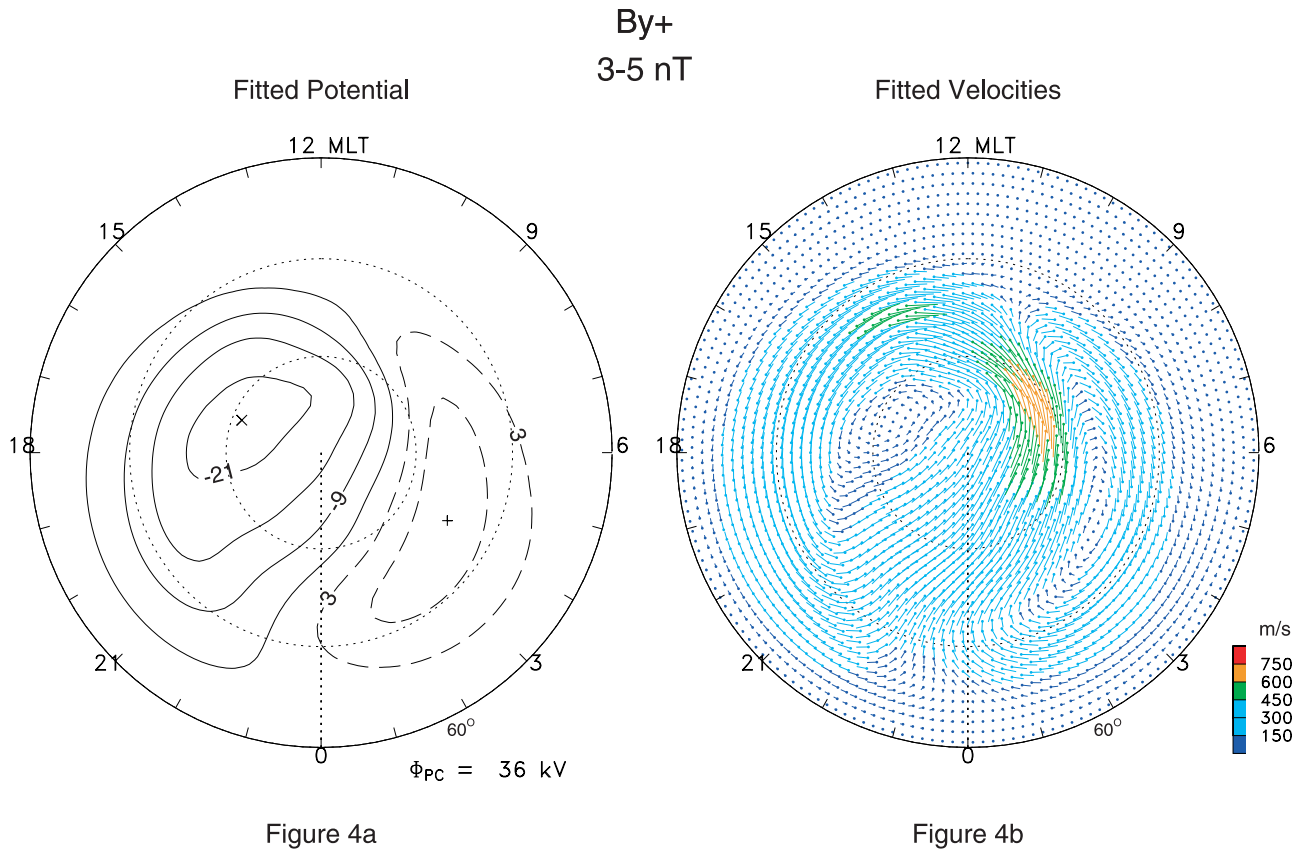

Figure 4a Figure 4b

Figure 4. (a) Map of the distribution of the electrostatic potential, Φ, obtained by fitting the velocity data of Figure 3 to an expansion of the potential in terms of spherical harmonic functions. (b) Map of convection velocity vectors implied by the solution for Φ.

account the more realistic boundary shape described by *Heppner and Maynard* [1987]. The Heppner-Maynard (H-M) boundary as defined by *Shepherd and Ruohoniemi* [2000] is circular on the nightside but withdraws to higher latitudes on the dayside. The distribution of HF backscatter usually conforms to this shape and thus provides us with a means of gauging the spatial extent of the convection zone. For this study we determined the H-M boundary for each data set by scaling the boundary according to the characteristics of the backscatter and velocity distributions. The latitude at which the boundary crosses the midnight MLT meridian, Λ_{HM}, identifies the setting. In the example of Figure 2a the H-M boundary corresponding to Λ_{HM} = 60 deg is shown by the dashed red curve. On the nightside the boundary is circular and coincides exactly with the zero potential boundary. In the fitting to obtain a potential pattern, the region on the dayside that is equatorward of the H-M boundary but poleward of the zero potential boundary contributes a set of zero velocity pads to the data set [*Shepherd and Ruohoniemi*, 2000] reflecting the expectation that this region is subauroral. In the example of Figure 2a the H-M boundary on the dayside corresponds to a steep decrease in counts with decreasing latitude and defines an edge to the zone of well-organized velocities. The principal impact of applying the H-M boundary condition on the fitting is to prevent the solution for potential contours from wandering into the dayside subauroral region. Appendix A lists the settings of Λ_{HM} that were obtained for the data sets considered in this paper.

[15] We note one important departure from the procedure described by *Ruohoniemi and Greenwald* [1998]. The fittings described here did not utilize statistical model data. In solving for instantaneous maps, for which the coverage provided by the radars is not truly global, a sparse set of velocity measurements from the model of *Ruohoniemi and Greenwald* [1996] is generally used to stabilize the results over areas of no observations. The exact selection of model data is keyed to the IMF. In this study, summing up the individual observations over many events typically results in very extensive coverage (e.g., Figure 2a) and no such stabilization is required.

4. RG05 Convection Model

[16] To obtain a basic characterization of the IMF dependencies of the convection, we have performed a standard binning by magnitude and clock angle in the GSM *Y-Z* plane. The magnitude intervals selected were 0–3, 3–5, and 5–10 nT. The step in clock angle was 45 deg and data were accepted for a solution if the direction of the associated IMF lay within 22.5 deg of the designated orientation. Thus a total of eight IMF orientations (B_z+, B_z+/B_y+, B_y+, B_z-/B_y+, B_z-, B_z-/B_y-, B_y-, B_z+/B_y-) were obtained per magnitude interval. We note that the stated magnitude intervals differ from those considered by RG96, which were 0–4, 4–6,

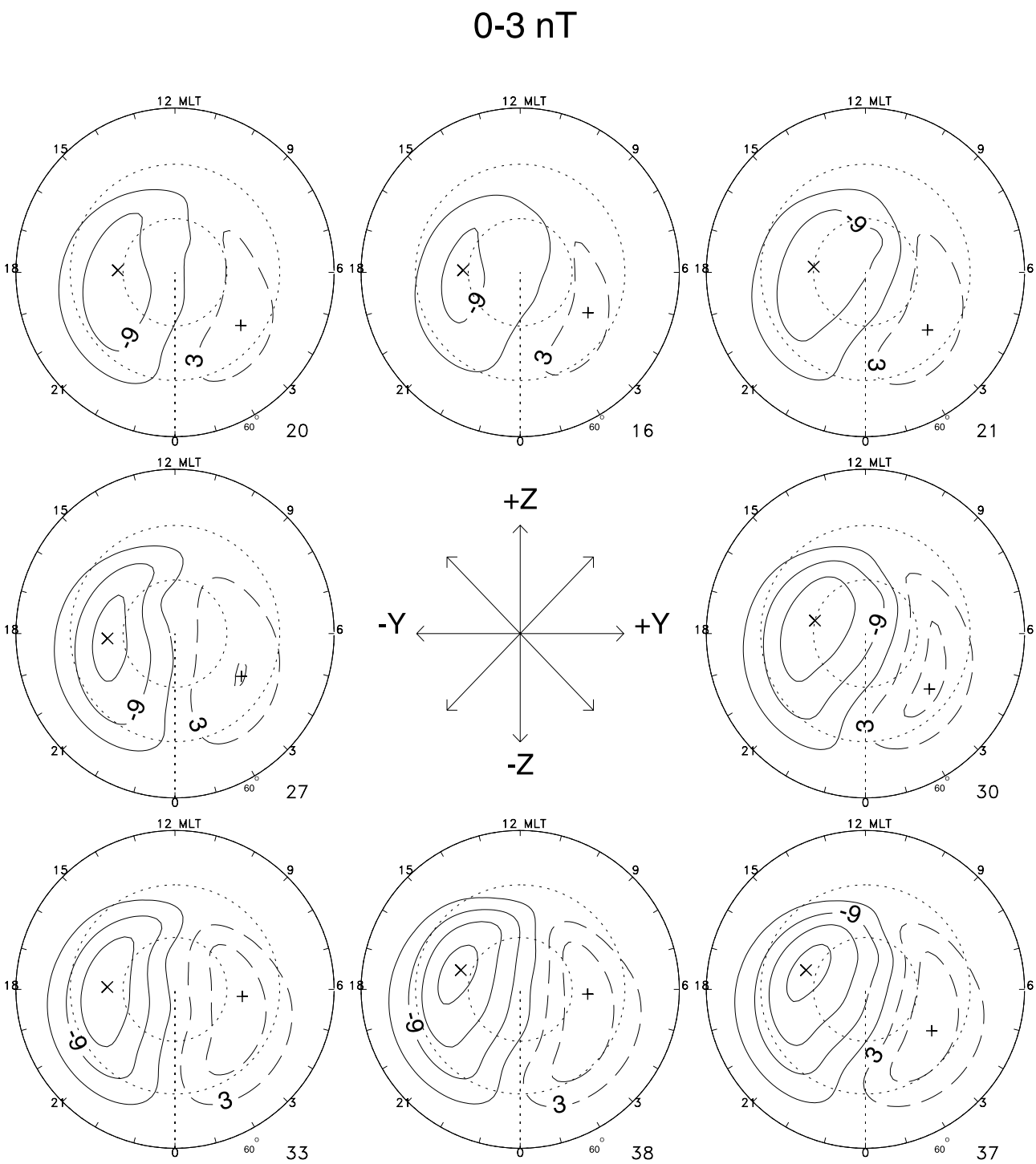

Figure 5. Statistical convection patterns sorted by clock angle in the GSM *Y-Z* plane for the 0–3 nT interval of IMF magnitude.

and 6–9 nT. We made this change in order to balance the occurrence statistics more evenly between the IMF magnitude intervals and to better resolve the IMF effects at smaller magnitude.

[17] The revised convection model, consisting of 24 patterns in total, is illustrated in Figures 5–7. This shows all the well-known dependencies, including the sculpting of the dawn and dusk cells into more rounded or crescent shapes depending on the sign of B_y, intensification of the two-cell pattern for increased magnitude of southward or azimuthal IMF, pronounced expansion of the pattern for increasing B_z-, and the emergence of sunward convection on the dayside for increasing B_z+. We also note the systematic rotation to later MLTs of the line joining the cell centers with progression of the IMF clock angle from B_y+ through B_z- to B_y-. Values of Φ_{PC} are consistently higher for B_y+ than for B_y-. Unsurprisingly, in the lowest interval of IMF magnitude the dependence

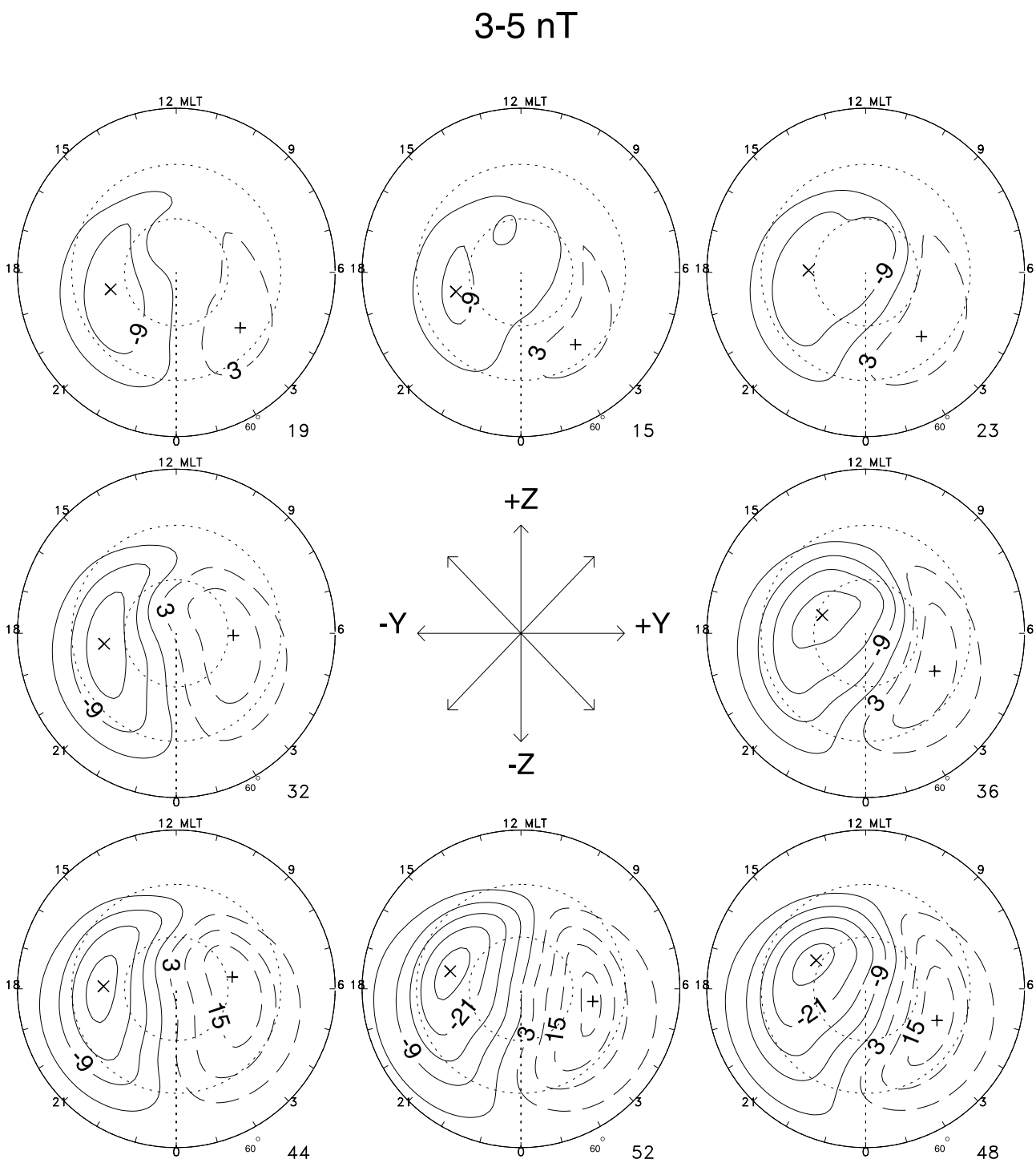

Figure 6. Statistical convection patterns sorted by clock angle in the GSM *Y-Z* plane for the 3–5 nT interval of IMF magnitude.

on clock angle is fairly muted and the pattern can be described as two-cell for all orientations with flow magnitudes that are roughly twice as large for B_z- as for B_z+. For the most expanded pattern, namely B_z- in the 5–10 nT interval, the centers of the convection cells still lie poleward of 70 deg latitude and hence the full magnitude of the antisunward flow across the polar cap can still be mapped by the SuperDARN radars and the estimate of Φ_{PC} remains well-determined.

[18] One other noteworthy aspect of the patterns is the appearance of a B_y- sign effect in the nightside convection. The sculpting of the cells into rounder and more crescent shapes persists into the nightside. The flows emerging from the polar cap in the vicinity of midnight skew toward the dusk (dawn) side for B_y+ (B_y-). Taking the crossover of the 70 deg latitude contour with the midnight meridian as a reference point, we see that with increasing magnitude of azimuthal IMF the crescent-

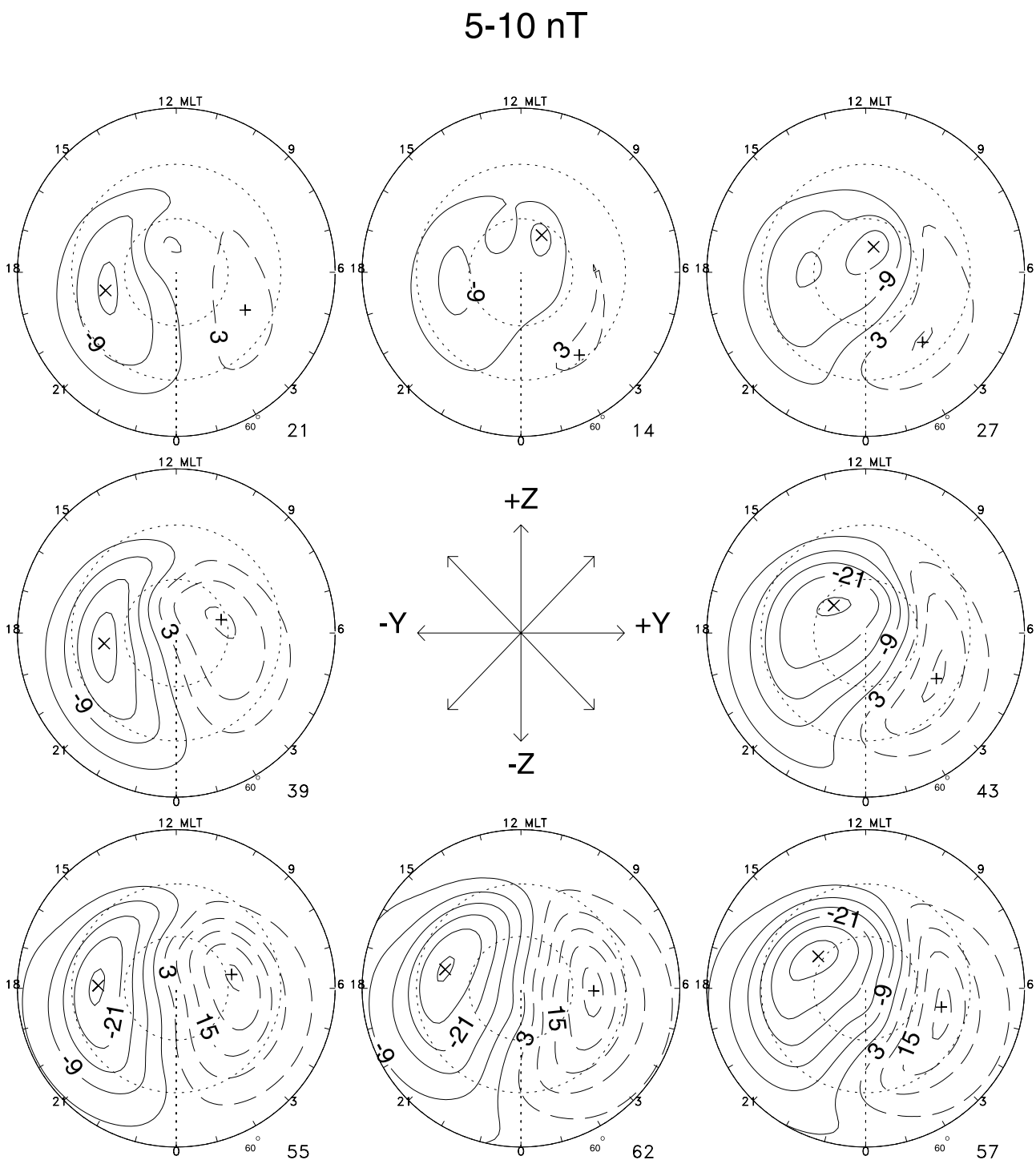

Figure 7. Statistical convection patterns sorted by clock angle in the GSM *Y-Z* plane for the 5–10 nT interval of IMF magnitude.

shaped cell extends further across the midnight sector. We conclude that the sign of IMF B_y has an impact on the average flows on the nightside that is almost as pronounced and systematic as that on the dayside. This set of patterns defines the RG05 convection model and replaces the RG96 model. A primary application of the HF-radar based models is to provide realistic background velocity data to support the reduction of radar measurements to instantaneous maps of the convection pattern, as described by *Ruohoniemi and Baker* [1998] and *Shepherd and Ruohoniemi* [2000].

5. Convection Dependencies

5.1. Seasonal Dependencies

[19] With the much larger data set of the RG05 model, we can explore the impact of sortings beyond those associated with the IMF. One factor that has been cited is season. The

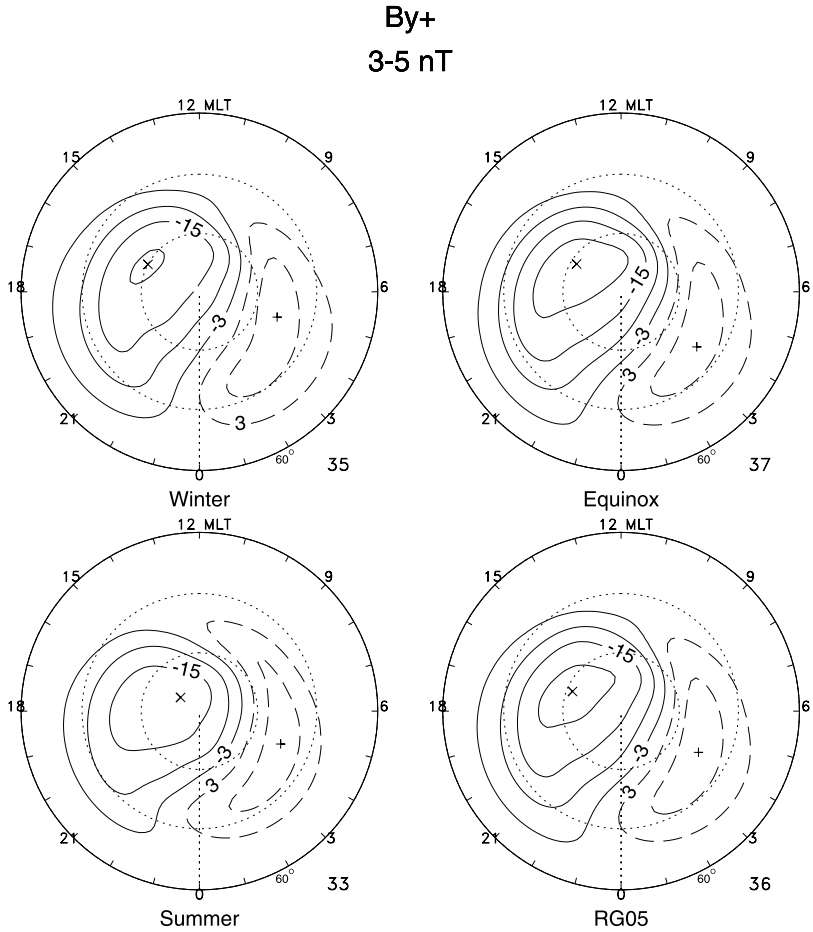

Figure 8. Statistical convection patterns sorted by season for predominantly IMF B_y+ conditions in the 3–5 nT interval of IMF magnitude. The corresponding RG05 pattern, which combines all seasons, is also shown.

first report of a seasonal dependence in the convection was due to *de la Beaujardiere et al.* [1991], who summed ion velocity data obtained with the Sondrestrom incoherent scatter radar and reported a larger potential drop in winter than in summer. The statistics of that study were insufficient to support simultaneous sortings by IMF and season, however. Subsequent satellite studies refined the description of the seasonal/dipole tilt factor [*Rich and Hairston*, 1994; *Weimer*, 1995] and an effect second-order compared with that of IMF was described. A limited radar study by *Ruohoniemi and Greenwald* [1995] reported a seasonal effect in the nightside convection that somewhat mimicked the effect of B_y sign, with more extreme sculpting of the dusk and dawn cells for the combinations of B_y+/summer and B_y−/winter. *Milan et al.* [2001] described a seasonal factor in the B_y dependence of the dayside convection velocities observations with the SuperDARN radar at Hankasalmi.

[20] For the analysis described here, we initially selected intervals of 90-day length for the winter, spring, and autumn seasons. Since little difference was found between the results obtained for spring and autumn, we combined these data sets into one equinoctial "season" of length 180 days. The rate of backscattering is significantly lower in summer compared to the other seasons [*Ruohoniemi and Greenwald*, 1997], likely owing to the dampening effect of increased HF absorption in the *D* and lower *E* regions of the ionosphere. To compensate, we set the interval for capture of summer data to 150 days. Consequently, we can expect the resolved patterns to somewhat underestimate the seasonal effect for summer.

[21] Figure 8 shows the set of patterns found for B_y+ conditions and IMF magnitude in the 3–5 nT range. Recall that for this IMF orientation the dawn cell is more crescent-shaped and the dusk cell is more round. The most striking contrast with the mean pattern described by the RG05 model (also shown) is found with the summer pattern. Here, the dusk cell is distinctly more round and the dawn cell is more elongated, the skew of the flow across the midnight meridian is greater, and the flows associated with the elongated dawn cell extend further across the midnight meridian. The tendency of the summer season to reinforce the effect of B_y+ in the convection of the midnight sector was first described by *Ruohoniemi and Greenwald* [1995]. On the dayside the convection streamlines are also more severely sculpted into round and crescent shapes, indicating that the B_y/season effect is global. The potential drop, Φ_{PC} = 33 kV, associated with the "reinforcing" combination of B_y+/summer is low relative to the other combinations of B_y+ with season.

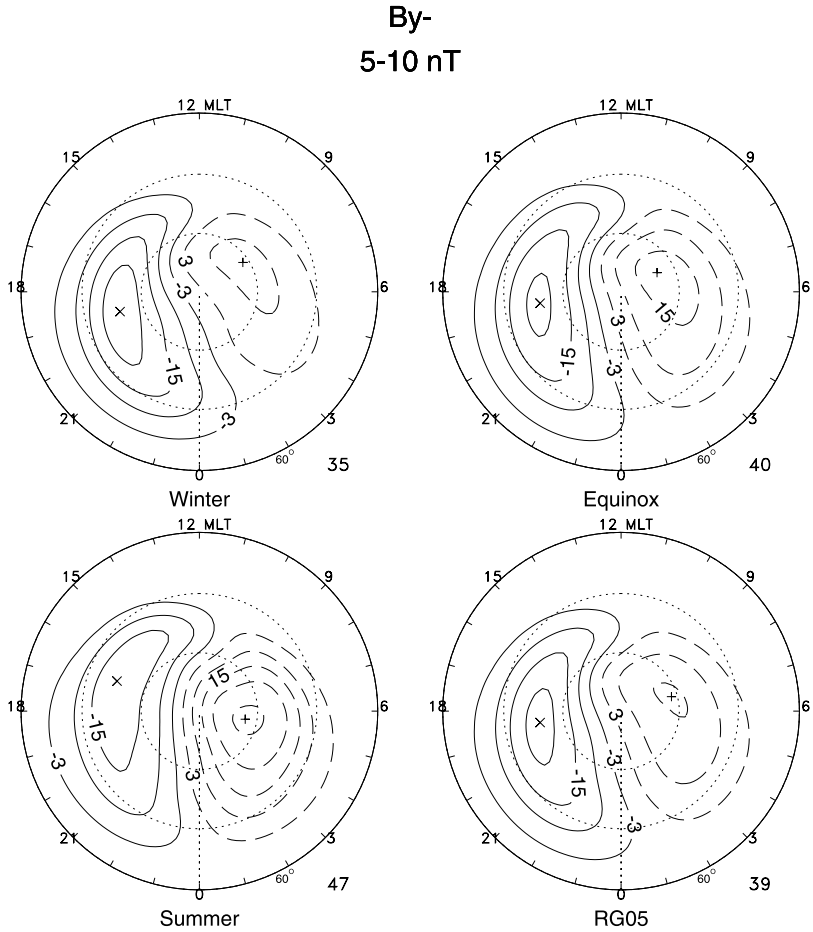

Figure 9. Statistical convection patterns sorted by season for predominantly IMF B_y- conditions in the 5–10 nT interval of IMF magnitude.

[22] Figure 9 shows the same progression with season for B_y- conditions and IMF in the 5–10 nT range of magnitude. For this sign of B_y the dusk cell becomes more elongated with clear definition of a convection reversal boundary that extends from noon through dusk to the midnight sector. With advance of season from winter to summer, there is greater variation in the pattern than was seen in the case of B_y+ conditions. The most obvious development is the intensification of the dawn cell that reverses the usual dominance of the dusk cell over the dawn cell in terms of area and potential variation. The summer pattern also shows a pronounced rotation of the line joining the cell centers to earlier MLTs, so much so that it more closely resembles the RG05 B_y+ patterns in this respect.

[23] In a manner analogous to the situation for B_y+/summer, the combination of B_y- with winter shows enhanced B_y- character in the nightside convection. The flows across the midnight meridian are then the most skewed and the crescent cell extends furthest across the midnight sector. In addition, the potential drop is suppressed relative to that of the associated RG05 pattern (35 kV versus 39 kV). Thus we find that the combinations of B_y+/summer and B_y-/winter, for which B_y- sign and season are reinforcing in terms of their sculpting effects on the convection, are associated with reduced values of Φ_{PC}.

[24] Another surprising result is the elevated potential drop recorded for the nonreinforcing combination of B_y- and summer, i.e., 47 kV versus 39 kV. The impact of the pairings of B_y and season on Φ_{PC} can be reviewed with the aid of Table 2. The reinforcing combinations of B_y+/summer and B_y-/winter result in lowered values of Φ_{PC} for all three IMF magnitude intervals. The nonreinforcing combination of B_y+/winter leads to values of Φ_{PC} that are basically equal to those of the associated RG05 patterns and higher than those of the reinforcing combinations. The nonreinforcing combination of B_y-/summer results in markedly larger Φ_{PC}. For an IMF in the 5–10 nT interval the potential drop for B_y- in summer is 47 kV versus 35 kV in winter. For B_y- conditions the change from winter to summer is sufficient to boost Φ_{PC} over its average value by as much as the increase incurred in stepping up by one interval in IMF magnitude.

[25] Table 2 also shows the results for seasonal pairings with B_z- and B_z+. These indicate that Φ_{PC} is generally elevated in summer. We can thus identify the following tendencies in the convection: (1) higher Φ_{PC} for the nonreinforcing B_y/season combinations and (2) higher Φ_{PC} in summer.

[26] The highest values of Φ_{PC} occur for B_y-/summer, for which the two tendencies act in the same sense. The impact of the B_y/season factor appears to be as large or larger than

Table 2. Φ_{PC} for Secondary Sorting by Season Versus Φ_{PC} for IMF Sorting Only (RG05) in kV

	IMF Magnitude in the GSM Y-Z Plane		
IMF/Season	0–3 nT	3–5 nT	5–10 nT
B_y+/winter	29 (30)	35 (36)	43 (43)
B_y+/summer	29 (30)	33 (36)	41 (43)
B_y−/winter	23 (27)	28 (32)	35 (39)
B_y−/summer	32 (27)	40 (32)	47 (39)
B_z−/winter	39 (38)	52 (52)	60 (63)
B_z−/summer	43 (38)	57 (52)	67 (63)
B_z+/winter	13 (16)	14 (15)	13 (14)
B_z+/summer	18 (16)	17 (15)	16 (14)

that of season alone, as the B_y+/winter and B_y+/summer pairings lead to values of Φ_{PC} that are equal to and lower than those of the associated RG05 patterns, respectively, despite the countervailing effect of season. The minimum values of Φ_{PC} are obtained when the suppressive factor of reinforcing B_y/season combines with that of season alone, i.e., B_y−/winter.

[27] We consider the origin in the convection pattern of the B_y/season factor. As noted for B_y− conditions (e.g., Figure 9), with advance of season from winter to summer Φ_{PC} increases and the convection pattern rotates to earlier MLTs (Figure 9). In terms of potential variation, the pattern progresses from domination by the dusk cell to domination by the dawn cell. A closer examination reveals that most of the change occurs in the dawn cell where both the area covered and the magnitude of the flow velocities (implied by the density of the potential contours) increase significantly. For B_y+ conditions (e.g., Figure 8), the relationship between the cells is much less sensitive to change of season and the flow velocities do not vary dramatically. Thus the seasonal effect in the convection that is linked to the sign of B_y is larger for B_y− conditions and its source lies mainly on the dawn side. The impact of the B_y/season factor on the convection is comparable to that of the variations in IMF magnitude and direction found in the discrete sampling of the RG05 and other statistical convection models.

5.2. Yearly Dependence

[28] We consider the possibility that the high-latitude convection exhibits year-to-year variations. It is known that ionization densities in the ionosphere fluctuate widely with variation in the 10.7 cm solar radio flux and that this factor has a strong dependence on the 11-year solar cycle. *Ruohoniemi and Greenwald* [1997] attributed a significant yearly variation seen in the backscattering occurrence statistics of the RG96 database to the impact of solar cycle factors. The variability in the ionosphere that arises from solar cycle factors could impart a secular variation to the convection pattern. Given the length of the solar cycle it seems appropriate to search for evidence of such a variation on a yearly basis. We note that the RG05 database encompasses 2 years of increasing solar activity (1998–1999), 2 years of peak activity (2000–2001), and 1 year of declining activity (2002).

[29] Figure 10 shows the results obtained for B_y+ in the 3–5 nT range of IMF magnitude for each calendar year. The pattern for the RG05 model (obtained by summing and averaging over all the years) is shown for comparison. The immediate impression is that the pattern is remarkably the same from year to year. This stability can be contrasted with the acute sensitivity of the pattern to IMF and seasonal factors that we have already discussed. An analysis (not shown) of the location of the convection reversal boundaries in the two cells reveals essentially no differences. The value of Φ_{PC} varies by only 2 kV (35–37 kV), which, in light of rounding off to obtain integer values, cannot be considered significant. The constancy of the pattern seen in Figure 10 is typical of the results for all 24 sets of IMF sorting conditions. As something of a contrary example, we show in Figure 11 the yearly variation for B_y− in the 5–10 nT range of IMF magnitude. Here, the value of Φ_{PC} varies over 7 kV (36–43 kV). A close inspection reveals that the size and configuration of the pattern change little from year to year. The variable part of the potential is due mostly to fluctuating magnitude of the dawn cell but represents in any case less than a 10% variation about the RG05 value of 39 kV. There is no sensible trend in the variation of Φ_{PC} with phase of the solar cycle. The slight year-to-year differences are likely due to fluctuations in the occurrence statistics within the IMF sorting intervals. We thus conclude that through the 5 years that bound the peak of the solar cycle, the dependence of the mean convection pattern on year or phase of the solar cycle is minor compared to those of the IMF and season.

5.3. Radar/UT Dependence

[30] Finally, we consider the possibility that the results for a statistical convection pattern derived from individual radar data sets might vary. This could arise from a UT dependence in the coupling of electric fields between the magnetosphere and ionosphere. Because of the offset of the geomagnetic pole from the rotational axis, observations carried out over the course of a day at a fixed position in (MLT, Λ) coordinates will be associated with a range of geographic latitudes and hence with different conditions of solar illumination and ionospheric conductivity. The offset between geographic and geomagnetic latitude varies from 0 deg in the Kodiak sector, through −10 deg in the Kapuskasing sector, to +4 deg in the Hankasalmi sector while all three radars are sited at nearly the same geomagnetic latitude (59 ± 2 deg). The cusp, which is located at a mean latitude of 78 deg Λ [*Newell and Meng*, 1992], will be observed at geographic latitudes that range from 68 deg to 82 deg over the course of a day. We search for a UT dependence in the convection by examining the patterns derived from the data sets of the individual radars.

[31] Factors peculiar to individual radars might also cause differences. One such known factor is variation in the latitudinal coverage provided by the radars. The Iceland radars in particular are located at relatively high geomagnetic latitude (∼65 deg Λ) and are oriented more zonally than the others. Consequently, the observations with these radars do not extend to the equatorward limit of the convection zone under conditions of even moderate expansion and also do not extend to the pole. (The effective poleward limits of coverage are 85 deg for Stokkseyri and 80 deg for Pykkvibaer.) These limitations can be expected to adversely impact the results for

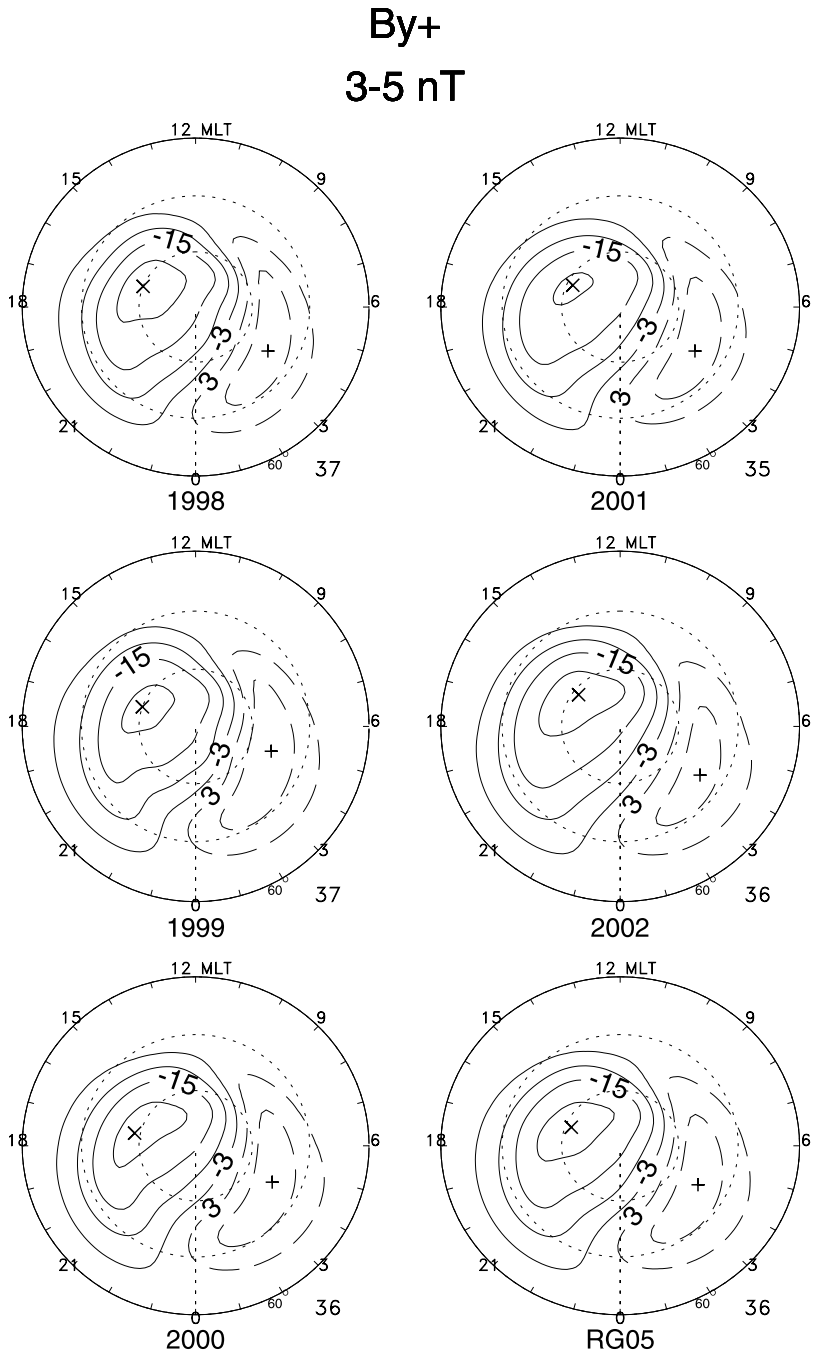

Figure 10. Statistical convection patterns sorted by year for predominantly IMF B_y+ in the 3–5 nT interval of IMF magnitude.

the global pattern determined from these radars. In addition, the data set of the westernmost radar at King Salmon (operational only since 2001) is insufficient to support a radar-specific derivation of IMF-sorted convection patterns.

[32] Figure 12 shows the convection patterns derived on the basis of the individual radar data sets for the case of B_y+ in the 3–5 nT range of IMF magnitude. The RG05 pattern (obtained by averaging over all the data sets) is also shown. (As expected, the patterns obtained from the data sets of the Iceland radars were less well constrained and their estimates for Φ_{PC} correspondingly unreliable. For these radars only partial maps of the distribution of equipotential contours are shown.) Overall, there is little evidence of a significant radar factor in the convection pattern. Any systematic trend with UT might be expected to peak for the Kapuskasing radar which observes the convection over the lowest range of geographic latitudes yet this pattern is essentially the same as those for the Kodiak and Hankasalmi radars. There is essentially no variation in the value of Φ_{PC}. Some slight variation in the positions of the cell centers can be perceived but these locations are not sharply defined by the potential

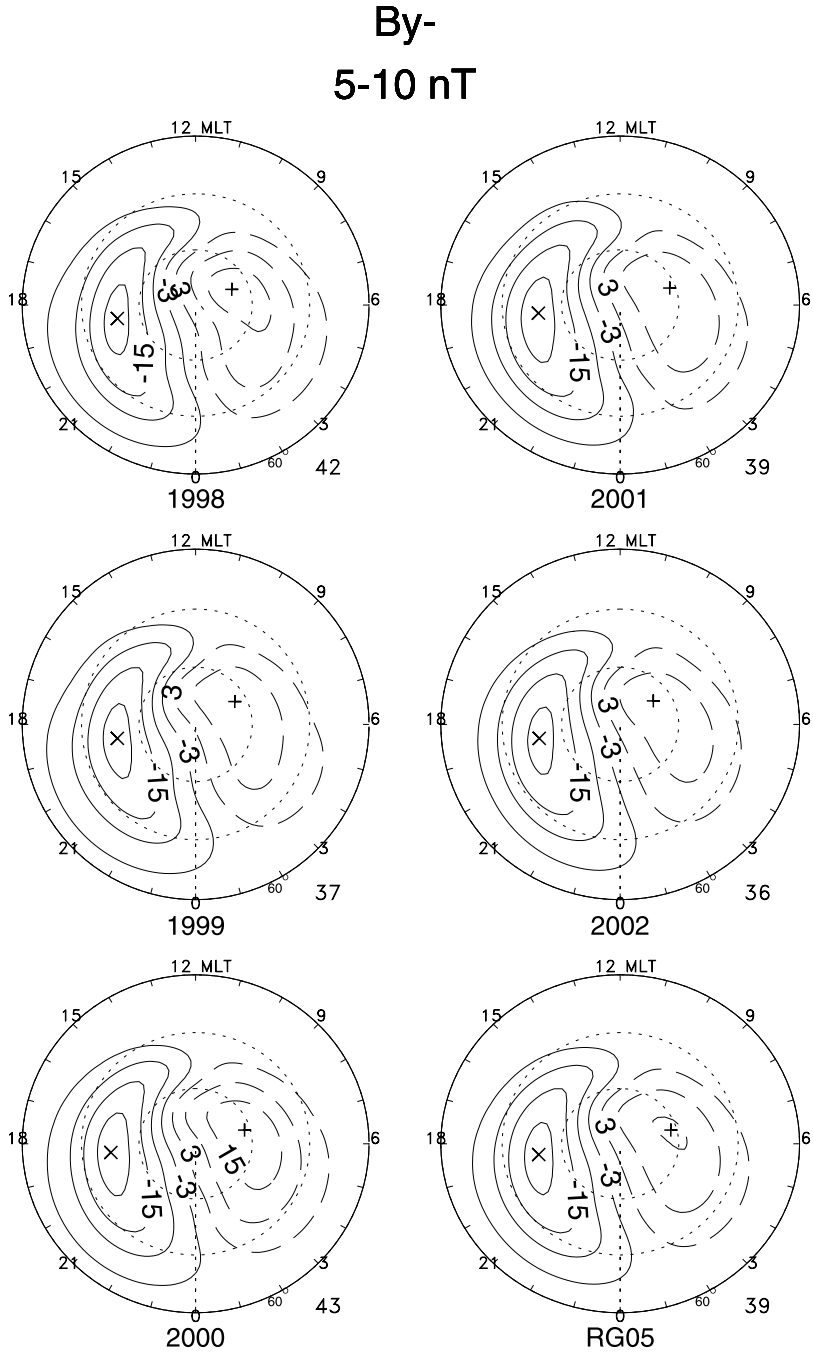

Figure 11. Statistical convection patterns sorted by radar for predominantly IMF B_y- in the 5–10 nT interval of IMF magnitude.

gradients along the convection reversal boundaries. Of greater significance is the fact that the locations of the CRBs themselves are very nearly the same from radar to radar. Examining the situation across the three intervals of IMF magnitude, we conclude that for predominantly B_y+ conditions there is no obvious radar (or UT) dependence in the convection pattern.

[33] The situation for B_y- in the same interval of IMF magnitude is shown in Figure 13. The configurations of the radar-specific patterns are again all broadly similar to that of the RG05 pattern. However, some surprising differences emerge between the western and eastern radars. The values of Φ_{PC} obtained from the Goose Bay and Hankasalmi data sets are relatively low, 32 and 27 kV respectively, compared with the 34–36 kV range of the three western radars. In terms of potential variation the dusk cell dominates the pattern for the central (Kapuskasing) and eastern radars while the dawn cell equals or exceeds the dusk cell for the western radars. Variability in the dawn sector makes the larger contribution to the variation. The value of Φ_{PC}

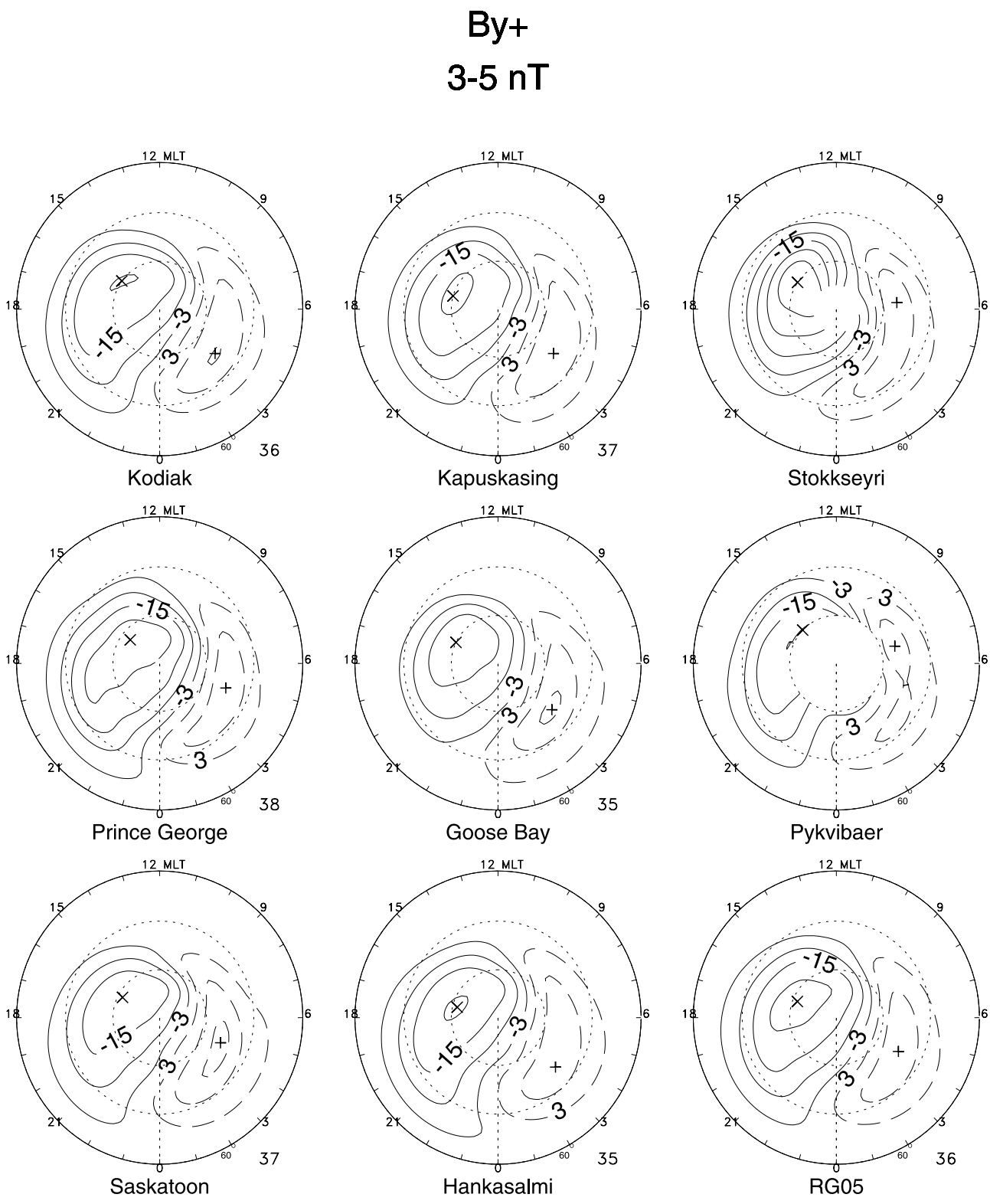

Figure 12. Statistical convection patterns sorted by radar for predominantly IMF B_y+ in the 3−5 nT interval of IMF magnitude.

obtained for the mean (RG05) statistical pattern, 32 kV, is notably low compared with the results for the radar-specific solutions, with only one radar (Hankasalmi) recording a lower value. This suggests some measure of inconsistent behavior in the contributing data sets.

[34] Rather than show another set of figures we comment briefly on the radar dependence of the patterns for B_z+ and B_z− conditions. The results for the B_z+ pattern are remarkably the same for all six radars that are capable of generating a global map. As shown in Figures 5−7, the

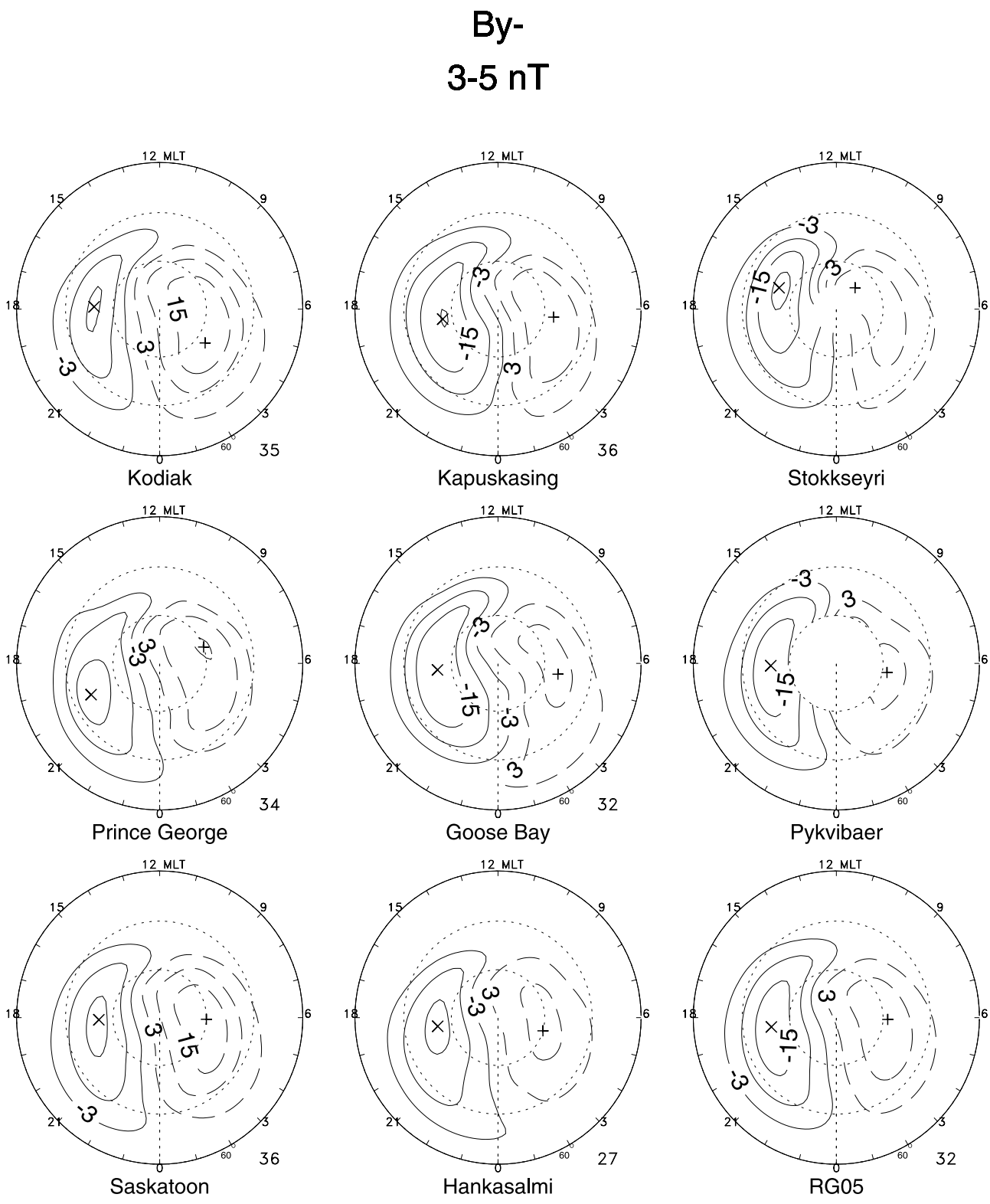

Figure 13. Statistical convection patterns sorted by radar for predominantly IMF B_y- in the 3–5 nT interval of IMF magnitude.

convection is weakly two-cell for small B_z+ but develops multicell character with the emergence of sunward flow on the noon meridian with increasing IMF magnitude. The value of Φ_{PC} for northward IMF averages 15 kV and varies over a limited range (12–17 kV). For B_z- conditions, there is again very good consistency between the patterns derived for the specific radars. As the IMF magnitude increases, the convection pattern expands beyond the field of view of the radars and greater uncertainties are incurred in the mapping results but there are still

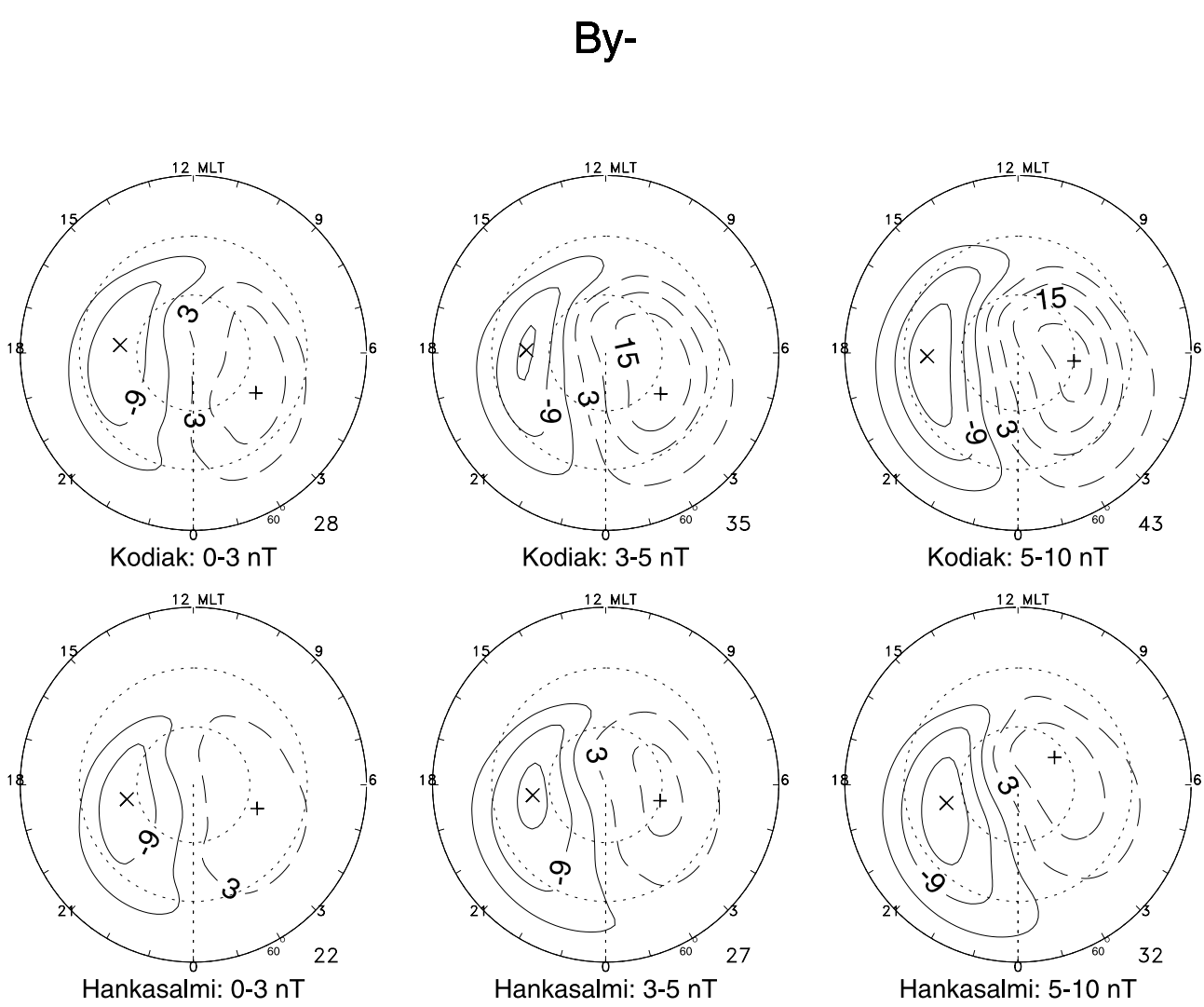

Figure 14. Progression of the statistical convection patterns derived for the Kodiak and Hankasalmi radars with increase in IMF magnitude for predominantly IMF B_y-.

no obvious radar dependencies. We find, however, that the RG05 estimates of Φ_{PC} for B_z- consistently underestimate the values obtained from the individual radars. For the three intervals of IMF magnitude considered we obtain 38 kV versus 38–43 kV, 52 kV versus 56–60 kV, and 62 kV versus 63–74 kV. We conclude that a pronounced radar dependence is not found for predominantly northward or southward IMF but there are some incompatibilities in the data sets for B_z-.

[35] We return to consideration of the singular case of B_y-. Figure 14 shows the progression in the convection pattern upon increase in IMF magnitude for the Kodiak and Hankasalmi radars. These radars lie at the furthest ends of the SuperDARN radar chain and their patterns express the differences between the results from the eastern and western portions most clearly. As expected, with increase in IMF magnitude the value of Φ_{PC} increases. For Hankasalmi, the dusk cell is always dominant and the increase in Φ_{PC} is shared roughly proportionately between the two cells. For Kodiak, the cells are almost equal for small IMF but the dawn cell intensifies more dramatically and dominates in the 5–10 nT interval of IMF magnitude. The greatest difference between the patterns is the asymmetry in the development of the dawn cell. The increase in Φ_{PC} with change of radar from Hankasalmi to Kodiak is as large as the increase incurred for a step of one in IMF magnitude interval. The radar dependence of the B_y- convection is thus as pronounced as the classical IMF dependencies.

[36] It is interesting that the differences between the radar-specific patterns of Figure 14 resemble the differences between the winter and summer patterns of Figure 9. Specifically, the Kodiak pattern shows more of the character of the B_y-/summer pattern and the Hankasalmi pattern more B_y-/winter character. This raises the possibility that the variation with radar is attributable to seasonal factors, or vice versa, due to bias in the backscatter occurrence statistics. To check on this, we have also derived patterns for the individual radars with a simultaneous sorting by season. The statistics are considerably reduced from those associated with the previous patterns and we do not complicate this presentation with the plots. For the

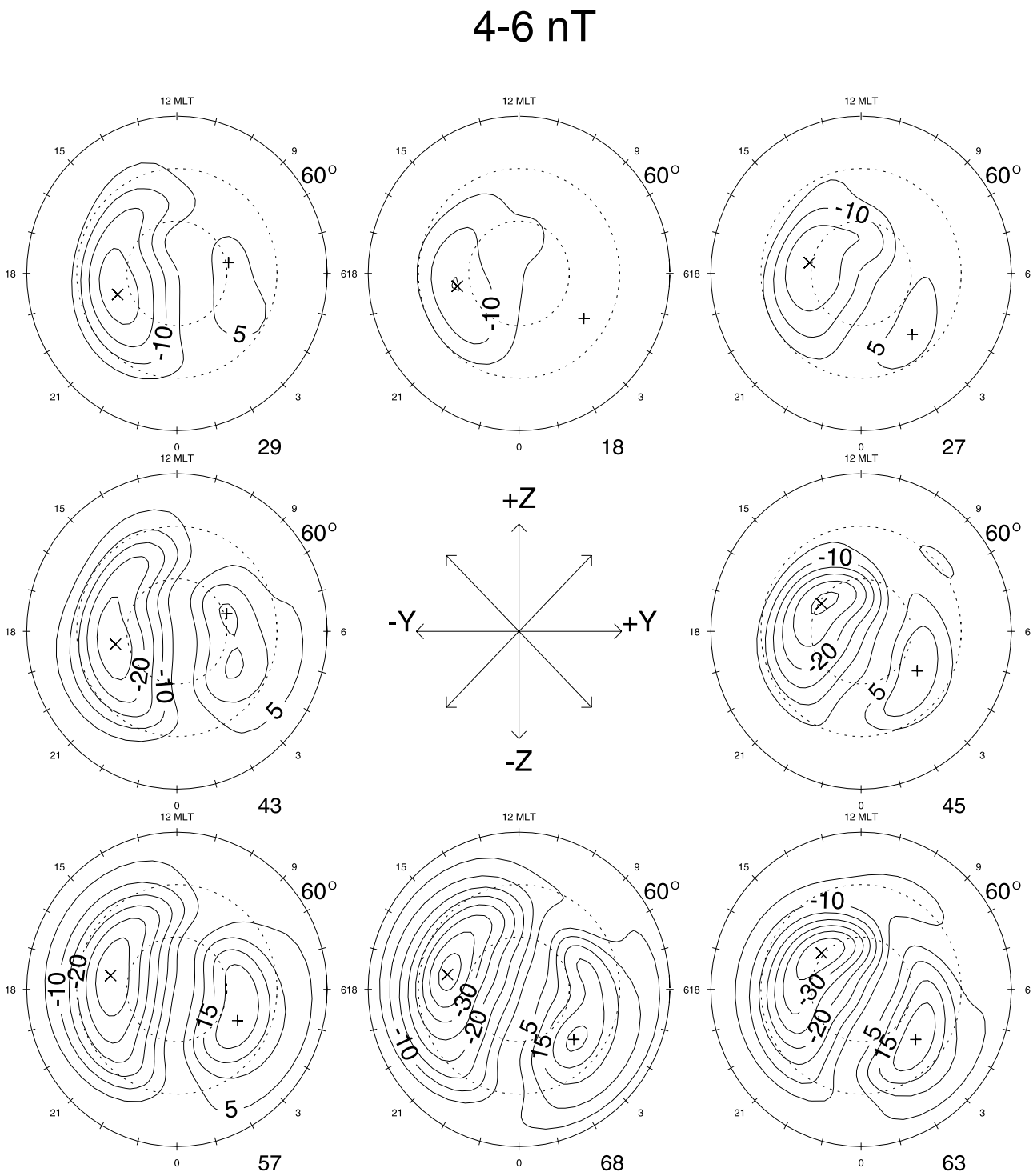

Figure 15. Statistical convection patterns of *Ruohoniemi and Greenwald* [1996] sorted by IMF clock angle in the GSM *Y-Z* plane in the 4–6 nT interval if IMF magnitude.

winter and equinoctial seasons the coverage suffices to confirm that the trends seen in Figure 13 and 14 are also seen within the seasonally sorted data. The radar factor is thus independent of the seasonal effect and comparable to it in magnitude.

[37] Summing over these results, we find very little variation among the patterns derived for individual radars for B_y+ conditions. However, there are pronounced differences among the B_y- patterns. These show a degree of organization by the UT factor in that the patterns derived from the radars located to the east and west of the central radar at Kapuskasing show common behavior. For B_z+ we obtain very similar results for all the radars while for B_z- there are somewhat greater uncertainties but also overall similarity. Indirectly, we sense a greater amount of variation in the results for B_z- in that these patterns of the RG05

model, which have been averaged over all the radar data sets, underestimate the values of Φ_{PC} obtained from the individual radar data sets.

6. Discussion

[38] The RG05 convection model can be compared with numerous other models. First we make a detailed comparison with its antecedent, the RG96 model.

[39] The earlier model was derived for a similar run of years centered on solar cycle maximum (1987–1993). For ease of comparison, we reproduce in Figure 15 the set of RG96 patterns for the 4–6 nT range of IMF magnitude. As noted earlier, the intervals of IMF magnitude chosen for the RG96 model, 0–4, 4–6, and 6–12 nT, differ from those adapted in the derivation of the new model. Since the occurrence of IMF magnitude falls off steeply beyond about 4 nT, the more appropriate comparison for RG96 in the 4–6 nT magnitude interval is the RG05 model in the 5–10 nT interval, i.e., Figure 15 with Figure 7. Overall, the patterns are quite similar. In the RG05 model the global shaping of the cells according to the sign of B_y is more pronounced and the dayside flows for B_z+ are more convoluted. This apparent improvement reflects a larger number of measurements and an increase in the order of the fitting from $L = 6$ to $L = 8$. The equipotential contours of the RG05 model show more curvature at higher latitudes. Because the earlier data set was incomplete above 85 Λ, a simple interpolation scheme was adopted to extend the mapping across the high polar cap; the improved coverage in the RG05 data set makes possible a more accurate depiction of these flows. There is an overall impression of greater consistency in the progression of cell size, shape, and orientation with IMF variation in the RG05 model. For example, the line joining the cell centers rotates more systematically in a counterclockwise sense as the IMF rotates from northward through $+Y$ to southward to $-Y$. The imposition of the Heppner-Maynard boundary condition on the fitting has kept the RG05 equipotentials from meandering unrealistically to subauroral latitudes on the dayside and suppressed the emergence of weak, extraneous cells there.

[40] There is a difference in the magnitude of the cross polar cap potential drop, or Φ_{PC}. Generally, Φ_{PC} is smaller in the RG05 model. This is seen in the comparison of Figures 7 and 15 despite the higher interval of IMF magnitude associated with the RG05 patterns. The reasons for systematically lower potential values are not clear, although minor differences in the reduction and processing of the two data sets may be a factor. We have also seen that inconsistencies between the radar data sets can suppress Φ_{PC} upon averaging. Allowing for this discrepancy, we observe very similar behavior in the two models, with generally greater Φ_{PC} for B_y+ than for B_y- and more potential variation across the dusk cell than the dawn cell.

[41] Comparable statistical models have been based on analysis of satellite data, e.g. *Rich and Hairston* [1994] and *Weimer* [1995], and magnetometers, e.g., *Papitashvili et al.* [1994] and *Ridley et al.* [2000]. Several of these have been upgraded into parameterized models that specify the convection pattern as a continuous function of solar wind variables, e.g., *Weimer et al.* [1996] and *Papitashvili and Rich* [2002]. These last authors also carried out a detailed comparison of the IMF and seasonal dependencies of Φ_{PC} reported in the current models. They concluded that the models are in good agreement in terms of the overall dependence on IMF magnitude and direction. The RG05 model somewhat improves upon the RG96 model in depicting the details of the convection pattern but is essentially consistent with this and the other models. The similarities are especially striking between the radar models and the earlier satellite-derived models.

[42] As discussed in the introduction, the value of the statistical models for prescribing the instantaneous pattern is degraded by the pronounced variability of the convection phenomenon. The averaged velocities do not show the full range of velocity magnitudes that are encountered in observations. The good agreement among the statistical models shows that there is nevertheless a background convection pattern for each IMF state that is reliably reproduced across a range of instrumental and analysis techniques. The instantaneous convection can then be interpreted in terms of the addition of transient convection features to a persistent global pattern of plasma circulation.

[43] There remains some disagreement regarding the magnitude of the convection as gauged by the value of Φ_{PC}. RG96 produced somewhat lower values of potential drop than the satellite models of the same vintage and the RG05 model clearly does not close this discrepancy. There is better agreement with the new satellite-derived DICM model of *Papitashvili and Rich* [2002]. Given the high level of consistency between the models in terms of the morphology of the pattern, it is perhaps surprising that a substantial variation in Φ_{PC} is reported. As an example, for B_y+ and an IMF magnitude of about 5 nT, Φ_{PC} ranges from 40 kV (DICM, RG05) to about 60 kV (e.g., *Weimer* [1995]). The spread in results for Φ_{PC} decreases for B_z+ and increases for B_z-.

[44] We have found a rather complicated dependence of the convection pattern on season. It has been usual to describe a general increase or decrease in Φ_{PC} with progression from winter to summer. We find it necessary to link season with the sign of IMF B_y to fully characterize the dependence. Stated simply, the combinations of B_y+/summer and B_y-/winter produce the most extreme configurations in terms of the round/crescent cell dichotomy and the shifting of the crescent cell across the midnight MLT meridian. The modulation of the convection on the nightside was first described by *Ruohoniemi and Baker* [1995] on the basis of very limited radar data. Here we see it confirmed on global scales and related to other dependencies. The nonreinforcing combinations of B_y-/summer and B_y+/winter lead to elevated values of Φ_{PC}. We find an overall tendency for Φ_{PC} to be larger in summer but the effect is not large enough to compensate for a contrary setting in the B_y/season combination. Thus the seasonal factor in isolation is of secondary importance to that of B_y/season.

[45] The first to describe effects in high-latitude convection specific to certain combinations of IMF B_y and season were apparently *Friis-Christensen and Wilhjelm* [1975]. They examined the dependence of magnetic variations in the polar cap. *Vennerstrom and Friis-Christensen* [1987] subsequently examined the dependencies of the polar cap

index *PC* and found the response maximizes for B_y-/summer and B_y+/winter. The data used in both studies of course incorporated the effects of dependencies in both the convection electric field and ionospheric conductivity but there is a telling coincidence with our findings of peak Φ_{PC} for these same combinations. These authors also called out the variable condition of the westward electrojet, which corresponds to our finding of greater variability in the dawn convection cell.

[46] Our results on the impact of season on convection can be compared more directly with those of the DICM model of *Papitashvili and Rich* [2002]. These authors described an overall decrease of 10–15% in Φ_{PC} in passing from winter to summer, which is the opposite sense of the seasonal effect that we have described. However, the seasonal variation of Φ_{PC} reported in the DICM study is also conditioned by the orientation of the IMF and, in the B_y- case, Φ_{PC} is larger in summer. It is also noteworthy that the convection pattern in the DICM model varies much more between the seasons for B_y- than for B_y+. We add that, in terms of overall configuration, our seasonal patterns for B_y+ are rather similar to those of the DICM model but the patterns for B_y- differ significantly, especially for B_y-/summer.

[47] The model of *Weimer* [1996] includes a sorting by dipole tilt angle that corresponds to season. The value of Φ_{PC} was found to increase from winter to summer for all orientations of the IMF. The sculpting effect of the reinforcing combinations of B_y/season on the shapes of the dawn and dusk cells is found in the *Weimer* [1996] patterns although it is less dramatic than in our results. Again, the variation of the pattern with season is greater for B_y-. The Weimer patterns show a peak value of Φ_{PC} for the nonreinforcing combination of B_y-/summer but not for the B_y+/winter combination. The Weimer model thus describes a seasonal effect on Φ_{PC} that is stronger than that of the combination of B_y- sign/season.

[48] *Milan et al.* [2001] analyzed line-of-sight velocity data collected with the Hankasalmi HF radar for evidence of a seasonal factor in the B_y dependence of dayside convection flows. They found a strong asymmetry between the convection response in summer and winter. In summer the velocities measured in the prenoon sector were strongly modulated by the sign of B_y, but not in winter, and less so in the postnoon sector. As the analysis was limited to the line-of-sight component of the convection velocity, it is not possible to easily characterize this result in terms of behavior the large-scale convection pattern but it is consistent with our finding of greater variability in the convection of the dawn cell. An inspection of the patterns of Figures 8 and 9 suggests that the dayside flows do vary more dramatically with a change in the sign of B_y in summer than in winter. We note that our results for specific radars showed that the convection observed from Hankaslami differs significantly from that seen with other radars for B_y- conditions; this might affect the generality of the findings obtained with this radar.

[49] *Crooker and Rich* [1993] considered the origin of the seasonal factor in the B_y dependence of the convection reported by *Rich and Hairston* [1994]. The observations had indicated that the dusk cell dominates the pattern, more so for B_y+, and still more for summer conditions. This was interpreted in terms of the impact of the quasi-permanent day-night conductivity gradient, the merging geometry on the dayside magnetopause, and the addition in summer of lobe cell convection to the dusk cell for B_y+. For B_y- the complementary addition of lobe cell convection to the dawn cell in summer was cited as the reason for the reduced dominance of the dusk cell. In our study we have found that indeed the dawn cell dominates the pattern for B_y- in summer. The corresponding total potential variation, Φ_{PC}, is much larger than in winter. Our results are more consistent than those of *Rich and Hairston* [1994] with the predictions of *Crooker and Rich* [1993], in that the addition of lobe cell convection should cause an intensification of the dawn cell for B_y- in summer and an increase in Φ_{PC} (*Rich and Hairston* [1994] obtained a decrease). However, the equivalent development with respect to B_y+ is not apparent in our results. In fact, the dusk cell is somewhat weaker in summer than in winter and Φ_{PC} is reduced. The same discrepancy was noted by *Crooker and Rich* [1993] in the results of *Rich and Hairston* [1994], although the dusk cell became more dominant as the result of an unexplained diminution in the dawn cell. We speculate that the lobe cell mechanism is more effective in enhancing convection for B_y- conditions in the northern hemisphere. This may be the source of the greater variability in the dawn sector reported here and in other studies.

[50] Although not presented here, we have also considered the seasonally sorted patterns for the slant IMF conditions of B_z+/B_y+ and B_z+/B_y-. As expected, these show a more pronounced development of possible lobe cell convection in summer than the pure B_y+ and B_y- cases and the corresponding cell (dusk or dawn) is enhanced over winter for the positive as well as the negative sign of B_y. However, the intensification of the dawn cell for negative sign of B_y remains much more dramatic.

[51] An asymmetric occurrence of lobe cell convection will give rise to hemispheric differences in the cross polar cap potential drop. Such differences are implied by our results, most dramatically for combinations of B_y and season, as expected, but also for season alone. Indeed, for predominantly B_z- conditions, the potential drop in summer exceeds that in winter by about 10% (Table 2). The contribution to the potential drop from merging processes that open and close field lines must be the same for both hemispheres. If the southern hemisphere experiences the same seasonal variation in total potential drop for B_z- conditions, the resulting hemispheric asymmetry must have a source in continued lobe cell circulation or in a seasonal effect in the viscous interaction along the magnetospheric flanks. *Crooker et al.* [1998] have argued that lobe cells are a consequence of merging site asymmetries. As these are a general feature of solar wind–magnetosphere coupling, they might occur in combination with merging cells even for a negative sign of B_z. Examination of the seasonal factors will be eventually be aided by comparison of these northern results with those obtained in the southern hemisphere with the Antarctic suite of SuperDARN radars.

[52] *Newell et al.* [1996] showed that ionospheric conditions related to variable solar illumination affects the precipitation of auroral particles. Subsequent studies have examined the roles of season and solar cycle factors on auroral particles and field-aligned currents, e.g., *Morooka*

and Mukai [2003]. Although the circumstances of the coupling of the solar wind and the magnetosphere have primary importance, it is becoming increasingly clear that variability in the ionosphere also impacts the system of electric fields, particle acceleration, and currents.

[53] *Tanaka* [2001] utilized a numerical MHD simulation to examine the interplay of IMF and ionospheric conductivity on convection. He found that when the conductivity is taken to be uniform, there is mirror symmetry in the patterns with respect to B_y. A realistic ionospheric conductivity modifies the pattern such that in the northern hemisphere, the distinctive features of the B_y+ pattern are enhanced. Furthermore, the flows at auroral latitudes in the midnight sector become more dominated by the crescent cell. *Tanaka* [2001] did not explicitly consider seasonal variations in conductivity but his results show that the IMF B_y factor should strongly influence convection on the nightside. Although *Tanaka* [2001] was apparently unaware of the findings of *Ruohoniemi and Baker* [1995], he reported in very similar terms that the impact of B_y on the convection was "accentuated" (reinforced) by the introduction of a realistic ionospheric conductivity. This suggests that the explanation of the seasonal factor in our observations is related to ionospheric conductivity. To the findings of *Ruohoniemi and Baker* [1995] we add that the reinforcing combinations of B_y and season are associated with lower values of Φ_{PC} while the nonreinforcing combination of B_y−/summer produces an anomalously high Φ_{PC}. The larger part of the seasonal variation for B_y− conditions was due to variability in the flows of the dawn convection cell. *Tanaka* [2001] argued that the ionospheric convection pattern should be considered the synthesized effect of magnetospheric and ionospheric factors. Specifically, the projection of the plasma convection from the magnetosphere needs to be balanced with the requirement of field-aligned current closure in the ionosphere. The B_y asymmetry in the nightside convection in particular is attributed to the condition of closure of ionospheric Hall current. We propose that one more test in the application of the numerical simulation will be to reproduce the seasonal dependencies.

[54] *Noda et al.* [2003] recently described the average B_y dependence of convection in the near-Earth tail lobe using measurements from the Cluster/EDI instrument. They found that the sense of velocity shear in the *Y-Z* plane reverses with a change in the sign of B_y in a manner consistent with the results of *Ruohoniemi and Greenwald* [1995]. Thus the impact of IMF orientation on nightside convection that we have more fully characterized with the RG05 database is substantiated by both MHD simulation and direct satellite observation. Our findings further show the presence of a comparable seasonal factor in the convection. Although we find a tendency for the potential to be larger in summer, the more significant, and surprising, seasonal impact depends on the IMF, especially the sign of B_y. Consideration of the role of ionospheric conductivity, possibly modulated by transport processes, may provide the key to understanding these dependencies.

[55] We note in passing that the patterns of Figure 8 show evidence of the impact of ionospheric conductivity on the convection pattern. As discussed by *Atkinson and Hutchinson* [1978], the conductivity gradient that is associated with the day-night terminator results in a deflection of the antisunward flow of the polar cap toward the duskside. For B_y+ conditions the effect is to enhance the shaping of the dusk and dawn cells [*Crooker and Rich*, 1993]. With progression of season from winter to summer, Figure 8 shows that the turning of the antisunward flow to distinctly duskward shifts across the polar cap in a manner consistent with the movement of the terminator, suggesting that this significant feature of the convection is controlled by the ionosphere.

[56] We have determined that the average convection pattern showed very little variation from year to year in the period 1998–2002. The stability of the patterns is remarkable, considering that the IMF and seasonal dependencies are so pronounced that even a small amount of skewing within the yearly statistics for a given IMF condition would be enough to produce significant differences with the mean pattern. The implication is that variability in the ionosphere related to solar cycle does not have a major impact on the average global convection. Strictly speaking, we have demonstrated this result for the half of the solar cycle centered on solar cycle maximum and there is the possibility of effects on less than global scales.

[57] We have derived and compared statistical convection patterns for the individual radars. Our expectation was that the varying offset of geomagnetic and geographic latitude across the radar chain might give rise to a systematic UT dependence. Because of their more limited latitudinal coverage, the Icelandic radars (Stokkseyri and Pykkvibaer) were less useful for this study. Overall, the statistical patterns derived for the other radars were similar. This result is somewhat reassuring in that it demonstrates the essential equivalence of the radars for mapping convection. The case of B_y− turned out to be exceptional, as a dependence could be made out in the variation of Φ_{PC}, namely, higher/lower values to the west/east of the central radar at Kapuskasing. The difference could be traced largely to the condition of the dawn cell, which has a greater presence in the observations of the western radars where it intensifies very rapidly upon increase in IMF magnitude. There is a dramatic contrast between the results for B_y+, where no radar dependence can be discerned, and B_y−, for which the radar dependence is as pronounced as those of the classical IMF dependencies.

[58] Why should a UT dependence emerge for B_y− but not for the other orientations of the IMF? More generally, why are the results for B_y− convection more variable with change of season or radar? If one were to appeal to the conductivity factor to explain this surprising aspect of the B_y dependence, the relation of the convection geometry to ionospheric conductivity gradients may be the key. The distinctive transformation of the convection pattern that occurs upon rotation of the IMF from B_y+ to B_y− consists of (1) enlargement of the dawn cell relative to the dusk cell, (2) reversal in the shaping of the dawn/dusk cells from crescent/round to round/crescent, (3) rotation of the overall pattern to later MLTs, and (4) displacement of the pattern duskward along the dawn-dusk meridian. We have observed that the flows in the dawn sector appear to be more variable than those in the dusk sector. Detailed consideration of the interplay of realistic ionospheric conductivities and the convection is beyond the scope of this paper. However, it

is interesting to note that for B_y+ the dawn cell is strongly crescent shaped and displaced to distinctly lower latitudes; the center of the cell lies at least 5 deg lower in latitude for B_y+ than for B_y−. Hence for this sign of azimuthal IMF the dawn cell is strongly constrained by the circumstances of solar wind−magnetosphere coupling which in this case favors reconnection on the duskside. For B_y− the geometry of the dawn cell is less constrained by the coupling factors and so conductivity variations may play a larger role. For this sign of B_y reconnection in the northern hemisphere is favored on the dawnside and at MLTs that are closer to the dawn-dusk line, and hence the conductivity gradient that is associated with the terminator, than is the case for B_y+. This could provide a basis for conductivity factors to impact the convection more for B_y− conditions. We found the sharpest contrast in the statistical patterns between summer and winter for B_y−. Across the radar chain the variation in the offset of geographic and geomagnetic latitude alters the relationship of the ionospheric conductivity to the convection pattern over the course of a day but the impact is similarly limited to conditions of B_y−.

[59] Our results have been obtained from observations carried out exclusively in the northern hemisphere. The seasonal variations in particular imply the existence of significant hemispheric asymmetries. An extensive database of measurements that is being accumulated by SuperDARN radars in the southern hemisphere will eventually provide a basis for examining conjugacy and help to resolve the impact of ionospheric factors on convection.

7. Summary

[60] Using the entire data set of velocity measurements collected with the northern SuperDARN radars over the years 1998−2002, we have derived a new statistical model of convection in the high-latitude ionosphere. The model replaces that derived by *Ruohoniemi and Greenwald* [1996] on the basis of data from the Goose Bay radar alone. The classic dependencies of the global convection on the magnitude and direction of the IMF in the GSM *Y-Z* plane are reproduced. We have also tabulated the size of the convection zone as a function of IMF settings used in the model.

[61] The database of the new model was then analyzed for information on the other dependencies of the convection. We extended to global scales the finding of *Ruohoniemi and Greenwald* [1995] that the seasonal effect is similar to that of the sign of B_y. In summer, the convection associated with B_y+ is composed of more severely shaped round and crescent cells in the dusk and dawn sectors, respectively, and the dawn cell protrudes further across the midnight meridian. In winter, the complementary situation for B_y− is realized, with more severe shaping of the of the crescent dusk cell and round dawn cell and a displacement of the dusk cell across the midnight meridian. These combinations of B_y sign and season "reinforce" the tendencies of the sign of B_y in terms of shaping the global pattern. The reinforcing combinations are, however, associated with lower values of the cross polar cap potential drop, Φ_{PC}. The nonreinforcing combinations of B_y sign and season lead to patterns that are intermediate in their morphology but have elevated values of Φ_{PC}. Overall, there is an increase in Φ_{PC} in going from winter to summer but the effect of season alone is smaller than that of the B_y/season factor. Most of the variability associated with the seasonal factor is found in the dawn cell.

[62] The database of the new model comprises 5 years for which the level of solar activity rose, peaked, and fell. We examined the IMF-sorted convection patterns derived for the individual years to search for a related secular variation but found nothing that rose to the level of significance of the IMF and seasonal dependencies.

[63] Finally, we considered the possibility of a dependence on radar. Such a dependence could arise from the variation in solar illumination and hence ionospheric conductivity across the convection pattern that accompanies the progression in UT of the magnetic pole about the rotational axis. For the six radars with sufficient coverage to map the global pattern, we found overall strong similarity in the results. Specifically, for B_y+, B_z+, and B_z− conditions no systematic dependence on UT could be discerned. However, differences were found for B_y−. These included lower values of Φ_{PC} for the radars to the east of the central radar at Kapuskasing and a pronounced difference in the behavior of the dawn cell.

[64] We speculate that the seasonal and UT dependencies of the convection are related to variable conductivity in the ionosphere. Sensitivities to ionospheric conductivity have been reported in the processes that control auroral particle acceleration in the magnetosphere [*Newell et al.*, 1996; *Morooka and Mukai*, 2003] and demonstrated in MHD modeling of convection in the ionosphere [*Tanaka*, 2001]. Our most surprising finding is that the impact of the seasonal and UT factors depends on the sign of B_y; they are pronounced for B_y− but hardly apparent for B_y+. This study and many others have demonstrated that the coupling of magnetic fields at the magnetopause is the primary factor in setting the global convection pattern. The IMF also appears to modulate the secondary role played by ionospheric conductivity.

Appendix A: Size of the Convection Zone Scaled by the Heppner-Maynard Boundary

[65] Table A1 lists the settings of the Heppner-Maynard (H-M) boundary as determined for the IMF conditions considered in this study. As discussed in relation to Figures 2 and 3, for each selection of IMF magnitude and direction in the GSM *Y-Z* plane the H-M boundary is adjusted until it encompasses the convection pattern determined from the radar data. The shape of the H-M boundary is fixed while its size is parameterized by the

Table A1. Reference Latitude of the Heppner-Maynard Boundary in Degrees

	IMF Magnitude		
IMF Direction	0−3 nT	3−5 nT	5−10 nT
B_z+	65	65	65
B_z+/B_y+	63	63	62
B_y+	62	60	58
B_z−/B_y+	61	59	56
B_z−	60	58	54
B_z−/B_y−	61	59	56
B_y−	62	60	58
B_z+/B_y−	63	63	62

latitude at which the boundary crosses the midnight MLT meridian [*Shepherd and Ruohoniemi*, 2000]. The step in latitude for the fitting to data is 1 deg. Two aspects of the radar data are chiefly examined: (1) the location of the equatorward edge of the zone of significant backscatter counts and (2) the spatial extent of sizeable, well-organized convective velocities. These boundaries largely coincide and the uncertainty in determining the location of the H-M boundary is about 1 deg. For B_z- conditions the fitting can only be performed on the dayside as the convection zone on the nightside then extends equatorward of the edge of the SuperDARN field of view. In this situation the radars do not directly observe the entire convection pattern. The solution for the global distribution of electrostatic potential will prescribe flows in the subhorizon region that are required to accommodate the flows seen at higher latitudes. We find that variation of a few degrees in the setting of the H-M latitude has little effect on the overall pattern or on the determination of Φ_{PC}.

[66] As expected, for strongly B_z+ conditions an increase in the magnitude of the IMF has little effect on the size of the convection zone. The size of the zone also does not depend appreciably on the sign of B_y. For a fixed IMF magnitude the pattern expands as the IMF vector rotates away from northward and especially when the sign of B_z turns negative. For strongly B_z- conditions, the latitude of the H-M boundary crossing on the midnight MLT meridian reaches as low as 54 deg and so a sizeable fraction of the return flows associated with the two-cell pattern then lies equatorward of the SuperDARN field of view.

[67] **Acknowledgments.** We gratefully acknowledge the support provided by NSF grant ATM-9819891 and by NSA grants NAG5-8361 and NAG5-8037. Operation of the SuperDARN radars in the northern hemisphere is supported by the national funding agencies of the US, Canada, UK, France, and Japan.

[68] Arthur Richmond thanks Stephen Milan and Takeshi Tanaka for their assistance in evaluating this paper.

References

Atkinson, G., and D. Hutchinson (1978), Effect of the day-night ionospheric conductivity gradient on polar cap convective flow, *J. Geophys. Res.*, *83*, 725–729.

Bristow, W. A., R. A. Greenwald, S. G. Shepherd, and J. M. Hughes (2004), On the observed variability of the cross-polar cap potential, *J. Geophys. Res.*, *109*, A02203, doi:10.1029/2003JA010206.

Crooker, N. U. (1979), Dayside merging and cusp geometry, *J. Geophys. Res.*, *84*, 951–959.

Crooker, N. U., and F. J. Rich (1993), Lobe cell as a summer phenomenon, *J. Geophys. Res.*, *98*, 13,403–13,407.

Crooker, N. U., J. G. Lyon, and J. A. Fedder (1998), MHD model merging with IMF B_y: Lobe cells, sunward polar cap convection; and overdraped lobes, *J. Geophys. Res.*, *103*, 9143–9151.

de la Beaujardiere, O., D. Alcayde, J. Fontanari, and C. Leger (1991), Seasonal dependence of high-latitude electric fields, *J. Geophys. Res.*, *96*, 5723–5735.

Dungey, J. W. (1961), Interplanetary magnetic fields and the auroral zones, *Phys. Rev. Lett.*, *6*, 47–48.

Friis-Christensen, E., and J. Wilhjelm (1975), Polar cap currents for different directions of the interplanetary magnetic field in the Y-Z plane, *J. Geophys. Res.*, *80*, 1248–1260.

Friis-Christensen, E., Y. Kamide, A. D. Richmond, and S. Matsushita (1985), Interplanetary magnetic field control of high-latitude electric fields and currents determined from Greenland magnetometer data, *J. Geophys. Res.*, *90*, 1325–1338.

Greenwald, R. A., W. A. Bristow, G. J. Sofko, C. Senior, J.-C. Ceriser, and A. Szabo (1995a), SuperDual Auroral Radar Network radar imaging of dayside high-latitude convection under northward interplanetary magnetic field: Toward resolving the distorted two-cell versus multicell controversy, *J. Geophys. Res.*, *100*, 19,661–19,674.

Greenwald, R. A., et al. (1995b), DARN/SuperDARN: A global view of high-latitude convection, *Space Sci. Rev.*, *71*, 763–796.

Greenwald, R. A., J. M. Ruohoniemi, K. B. Baker, W. A. Bristow, G. J. Sofko, J.-P. Villain, M. Lester, and J. Slavin (1999), Convective response to a transient increase in dayside reconnection, *J. Geophys. Res.*, *104*, 10,007–10,015.

Heppner, J. P. (1977), Empirical models of high-latitude electric fields, *J. Geophys. Res.*, *82*, 1115–1125.

Heppner, J. P., and N. C. Maynard (1987), Empirical high-latitude electric field models, *J. Geophys. Res.*, *92*, 4467–4489.

Milan, S. E., L. J. Baddeley, M. Lester, and N. Sato (2001), A seasonal variation in the convection response to IMF orientation, *Geophys. Res. Lett.*, *28*, 471–471.

Morooka, M., and T. Mukai (2003), Density as a controlling factor for seasonal and altitudinal variations of the auroral particle acceleration region, *J. Geophys. Res.*, *108*(A7), 1306, doi:10.1029/2002JA009786.

Newell, P. T., and C.-I. Meng (1992), Mapping the dayside ionosphere to the magnetosphere according to particle precipitation characteristics, *J. Geophys. Res.*, *19*, 609–612.

Newell, P. T., C.-I. Meng, and S. Wing (1996), Suppression of discrete aurorae by sunlight, *Nature*, *381*, 766–767.

Noda, H., W. Baumjohann, R. Nakamura, K. Torkar, G. Paschmann, H. Vaith, P. Puhl-Quinn, M. Forster, R. Torbet, and J. M. Quinn (2003), Tail lobe convection observed by Cluster/EDI, *J. Geophys. Res.*, *108*(A7), 1288, doi:10.1029/2002JA009669.

Papitashvili, V. O., and F. J. Rich (2002), High-latitude ionospheric convection models derived from Defense Meteorological Satellite Program ion drift observations and parameterized by the interplanetary magnetic field strength, *J. Geophys. Res.*, *107*(A8), 1198, doi:10.1029/2001JA000264.

Papitashvili, V. O., B. A. Belov, D. S. Faermark, Y. I. Feldstein, S. A. Golyshev, L. I. Gromova, and A. E. Levitin (1994), Electric potential patterns in the northern and southern polar regions parameterized by the interplanetary magnetic field, *J. Geophys. Res.*, *9*, 13,251–13,262.

Reiff, P. H., and J. L. Burch (1985), IMF B_y-dependent plasma flow and Birkeland currents in the dayside magnetosphere: 2. A global model for northward and southward IMF, *J. Geophys. Res.*, *90*, 1595–1609.

Rich, F. J., and M. Hairston (1994), Large-scale convection patterns observed by DMSP, *J. Geophys. Res.*, *99*, 3827–3844.

Ridley, A. J., G. Lu, C. R. Clauer, and V. O. Papitashvili (1998), A statistical study of the ionospheric convection response to changing interplanetary magnetic field conditions using the assimiliative mapping of ionosphgeric electrodynamics technique, *J. Geophys. Res.*, *103*, 4023–4039.

Ridley, A. J., G. Crowley, and C. Freitas (2000), An empirical model of the ionospheric electric potential, *Geophys. Res. Lett.*, *27*, 3675–3678.

Ruohoniemi, J. M., and K. B. Baker (1998), Large-scale imaging of high-latitude convection with Super Dual Auroral Radar Network HF radar observations, *J. Geophys. Res.*, *103*, 20,797–20,811.

Ruohoniemi, J. M., and R. A. Greenwald (1995), Observations of IMF and seasonal effects in high-latitude convection, *Geophys. Res. Lett.*, *9*, 1121–1124.

Ruohoniemi, J. M., and R. A. Greenwald (1996), Statistical patterns of high-latitude convection obtained from Goose Bay HF radar observations, *J. Geophys. Res.*, *101*, 21,743–21,763.

Ruohoniemi, J. M., and R. A. Greenwald (1997), Rates of scattering occurrence in routine HF radar observations during solar cycle maximum, *Radio Sci.*, *32*, 1051–1070.

Ruohoniemi, J. M., and R. A. Greenwald (1998), The response of high-latitude convection to a sudden southward IMF turning, *Geophys. Res. Lett.*, *25*, 2913–2916.

Ruohoniemi, J. M., R. A. Greenwald, K. B. Baker, J.-P. Villain, and M. A. McCready (1987), Drift motions of small-scale irregularities in the high-latitude F region: An experimental comparison with plasma drift motions, *J. Geophys. Res.*, *92*, 4553–4564.

Ruohoniemi, J. M., R. J. Barnes, R. A. Greenwald, and S. G. Shepherd (2001), The response of the high-latitude ionosphere to the coronal mass ejection event of April 6, 2000: A practical demonstration of space weather nowcasting with the Super Dual Auroral Radar Network HF radars, *J. Geophys. Res.*, *106*, 30,085–30,097.

Ruohoniemi, J. M., S. G. Shepherd, and R. A. Greenwald (2002), The response of the high-latitude ionosphere to IMF variations, *J. Atmos. Sol. Terr. Phys.*, *64*, 159–171.

Shepherd, S. G., and J. M. Ruohoniemi (2000), Electrostatic potential patterns in the high-latitude ionosphere constrained by SuperDARN measurements, *J. Geophys. Res.*, *105*, 23,005–23,014.

Tanaka, T. (2001), IMF By and auroral conductance effects on high-latitude ionospheric convection patterns, *J. Geophys. Res.*, *106*, 24,505–24,516.

Vennerstrom, S., and E. Friis-Christensen (1987), On the role of IMF By in generating the electric field responsible for the flow across the polar cap, *J. Geophys. Res.*, *92*, 195–202.

Villain, J. P., R. A. Greenwald, and J. F. Vickrey (1984), HF ray tracing at high latitudes using measured meridional electron density distributions, *Radio Sci.*, *19*, 359–374.

Villain, J.-P., G. Caudal, and C. Hauise (1985), SAFARI-EISCAT comparison between the velocity of F region small-scale irregularities and the ion drift, *J. Geophys. Res.*, *90*, 8433.

Weimer, D. R. (1995), Models of high-latitude electric potentials derived with a least error fit of spherical harmonic coefficients, *J. Geophys. Res.*, *100*, 19,595–19,607.

Weimer, D. R. (1999), Substorm influence on the ionospheric electric potentials and currents, *J. Geophys. Res.*, *104*, 185–197.

R. A. Greenwald and J. M. Ruohoniemi, Johns Hopkins University Applied Physics Laboratory, 11100 Johns Hopkins Road, Laurel, MD 20723-6099, USA. (mike_ruohoniemi@jhuapl.edu)